Journal of Petroleum Science and Engineering 213 (2022) 110466

Contents lists available at ScienceDirect

Journal of Petroleum Science and Engineering

journal homepage: www.elsevier.com/locate/petrol

Evolution of the mineralogy, pore structure and transport properties of Nordland Shale following exposure to supercritical carbon dioxide

Richard Seely [a,b], Thomas J. Liddy [c], Christopher A. Rochelle [c], Robin S. Fletcher [d], Sean P. Rigby [a,b,*]

[a] Department of Chemical and Environmental Engineering, University of Nottingham, University Park, Nottingham, NG7 2RD, UK
[b] Geo-energy Research Centre, University of Nottingham, University Park, Nottingham, NG7 2RD, UK
[c] British Geological Survey, Keyworth, Nottingham, NG12 5GG, UK
[d] Johnson Matthey, P.O. Box 1, Belasis Avenue, Billingham, Cleveland, TS23 1LB, UK

ARTICLE INFO

Keywords:
Caprock
Carbon sequestration
X-ray tomography
Bulk condensation
Pore network
Diffusion

ABSTRACT

The Nordland shale forms the caprock of the Utsira sands of the Sleipner reservoir currently used for carbon dioxide sequestration. The long-term exposure of shale rocks to supercritical carbon dioxide ($scCO_2$), or $scCO_2$-brine mixtures, may lead to structural and chemical changes in shale that lead to increases in permeability of inter-layers and caprocks, that may mean changes to plume migration behaviour and/or loss of seal efficiency of caprocks. A detailed study has been made of the initial pore structure of Nordland shale and the changes following accelerated treatment with $scCO_2$. Gas sorption scanning curves have suggested that the void space of the original shale consisted of a Network (denoted 1) of micropores and smaller mesopores that is thermodynamically independent of a Network (2) of larger mesopores and macropores. This work introduces a new iodononane pre-adsorption technique to map the macroscopic (>microns) spatial distribution of micropores (<2 nm) and smaller mesopores in shales using CXT. CXT imaging of shale samples with iodononane pre-adsorbed in Network 1, or with entrapped mercury confined to only Network 2, suggested that both small- and large-sized pore networks were pervasive through the shale and associated with the continuous illite matrix phase. The feldspar and quartz grains did not form part of either network, though inter-particle macropores were found surrounding these mineral grains from CXT imaging of mercury entrapped there. Kinetic gas uptake experiments conducted on samples before and after filling Network 1 with iodononane suggested that the smaller mesopores were, despite their small size and thermodynamic independence from the macropores, still critical to mass transport, with the diffusion flux being funnelled through them. Shale surface areas obtained using the homotattic patch adsorption model were found more physically realistic than those determined via the ISO BET method since multi-linear regression of only the logarithm of the former, together with that of the Network 1 pore volume, predicted the gas-phase mass transport coefficient following treatment. This work demonstrated the need for the novel characterisation methods and data analysis presented here to properly understand the structure-transport relationship in shales exposed to $scCO_2$.

1. Introduction

The impact on the pore structure and chemistry of mudrocks, such as shale, resulting from thermochemical treatments, such as exposure to supercritical carbon dioxide ($scCO_2$), is important to understand changes in rock adsorption and transport properties, in order to explain overall reservoir performance during processes such as $scCO_2$ sequestration. In this work, the changes to the pore network structure and mass transport properties of Nordland shale samples, as a result of accelerated exposure to $scCO_2$, will be used as a case study for deploying some new developments of established pore characterisation approaches, and also some entirely novel techniques introduced here. Pore sizes are classified by the IUPAC into micropores of sizes <2 nm, mesopores of sizes in the range 2–50 nm, and macropores of sizes >50 nm (Thommes et al., 2015; Rigby, 2020). Microporosity, commonly found in shales, is further subdivided into the very smallest ultra-micropores, where the

* Corresponding author. Department of Chemical and Environmental Engineering, University of Nottingham, University Park, Nottingham, NG7 2RD, UK.
E-mail address: sean.rigby@nottingham.ac.uk (S.P. Rigby).

https://doi.org/10.1016/j.petrol.2022.110466
Received 2 December 2021; Received in revised form 21 March 2022; Accepted 22 March 2022
Available online 26 March 2022

idiosyncratic micropore-filling process happens, and super-micropores with sizes between these and mesopores (Gregg and Sing, 1982).

In order to properly understand which pore structural changes actually impact mass transport it is necessary that these changes be characterised using reliable and accurate void space descriptors, and that these descriptors are explicitly predictive of mass transport parameters. While a broad range of types and sizes of void spaces within shales may be modified, or lost, by thermochemical processes, not all of them may be of importance to mass transport. In this work it will be seen that conventional void space descriptors, such as the standard BET surface area from the ISO (2010) method, are not accurate and therefore not capable of further predictive use. Instead, we propose characterisation methods for shales that can deliver void space descriptors tested as predictive for mass transport.

Shale rocks have complex, multi-scale pore structures. Different sizes and types of pores arise between and within different mineral phases of the rock, and over different length-scales (Loucks et al., 2012). The impact of the interactions with carbon dioxide may vary between these phases and/or length-scales. It is thus important to use pore structural characterisation tools that can probe these sorts of variability. Multi-scale imaging, using different modalities to probe different length-scales, has been used to characterise heterogeneous rocks (Saif et al., 2017; Ma et al., 2019). Computerised X-ray tomography (CXT) is used to probe larger length-scales (typically ~100 s nm and above), while dual-beam electron microscopy (such as focussed-ion beam (FIB) SEM) or electron tomography is used to probe smaller length-scales (Saif et al., 2017; Ma et al., 2019). However, particularly for the FIB-SEM, the field-of-view (FOV) possible for a single image is often smaller than the correlation length of the heterogeneities, and data-sets are thus unrepresentative of the overall porous structure (Arif et al., 2021; Holzer, 2010). It is often not clear just how many sampling trenches for FIB-SEM must be dug, and where, to provide a fully representative characterisation. Representative volume measurements at high resolution on a small FOV may be misleading because the multi-scale heterogeneity in shales means the pore structure may be quite different in other zones outside the particular FOV tested. The limits to the levels of practically feasible sampling often mean assumptions must be made concerning the number of different phases in the rock that are distinguishable, and the degree of homogeneity between instances of particular phases across the material. These issues also impact on the assessment of the inter-relationship between the different aspects of the pore structure probed by the different imaging modalities at different scales. Hence, there is a need for methods that can 'bridge' the wide range of length-scales found in shales from 100s microns down to molecular scale, including the inter-relationship between these levels.

Gas overcondensation and mercury porosimetry are the only pore characterisation techniques that can probe pore sizes ranging from hundreds of microns down to molecular dimensions, or nanometres, respectively, in one experiment (Rigby, 2018, 2020). While these techniques provide less direct, characterisations of pores than imaging methods, their sensitivity to sample-spanning, pore-to-pore co-operative effects means they can deliver statistically-representative information on the inter-relationship of pore networks of different sizes across macroscopic scales (Pitcher et al., 2021).

Gas sorption scanning has demonstrated great utility in probing the origins of sorption hysteresis and pore connectivity in porous catalysts (Tompsett et al., 2005). However, it is seldom used for characterising rocks (Seemann et al., 2017), and, even then, in only a few studies is it analysed in-depth (Barsotti et al., 2020; Rigby et al., 2020a; Pitcher et al., 2021). However, scanning can be used to segment complex void spaces into dissociable parts that are physically meaningful, unlike some abstract, model-based, pore size distribution and image analysis algorithms.

Indirect methods such as gas adsorption and mercury porosimetry can be combined with imaging methods to provide a synergistic hybrid characterisation method that combines some of the advantages of both direct and indirect methods (Rigby, 2020). In particular, the controlled ingress of probe species, visible to CXT (known as contrast agents), into only particular pore sizes achieved via gas sorption or liquid porosimetry, allows the probing of the macro- and micro-scopic length-scale variation in nanoscopic properties. Some CXT studies of rocks imbibed with contrast agents simply aimed at measuring only total porosity variation (Hellmuth et al., 1999; Mayo et al., 2015). While magnetic resonance (MR) image individual voxel contrast can be made sensitive to pore sizes within the voxel volume, via relaxometry (Rigby, 2020), CXT voxel X-ray absorption contrast cannot. However, the control, over accessible pore size, achieved in porosimetry methods means only the required pore sizes can be filled with X-ray contrast agent. Mercury and low-melting point alloys have been extensively used to probe mesopores and macropores in rocks (Rigby et al., 2020a; Klaver et al., 2015). Imaging of the kinetics of adsorption can also be performed with CXT, but X-ray absorption contrast arises overwhelmingly from the condensed phase, rather than the gas, due a factor of ~1000 difference in density (Pini et al., 2021). However, little or no work has been done on the macroscopic spatial distribution of micropores, especially those beyond the limits of resolution even via SEM, in rocks.

Shales can be exposed to $scCO_2$ in two key sub-surface operations. $scCO_2$ can be injected into aquifers, or old gas reservoirs, as a way to sequester carbon, and can also be used to displace methane from shale gas reservoirs. In aquifer storage of CO_2, an envisaged scenario would be for $scCO_2$ to be injected at the base of the reservoir, and, being less dense than the surrounding brine, it then rises up through the reservoir due to the action of buoyancy forces. All aquifers are heterogeneous to a degree. For example, the Sleipner field (in the Norwegian sector of the North Sea) has shale inter-layers amidst the more porous reservoir sandstone, which the $scCO_2$ encounters on its journey through the reservoir. The caprock providing the overall seal for a reservoir is also typically a mudstone like shale. The long-term exposure of shale rocks to $scCO_2$, or $scCO_2$-brine mixtures, may lead to structural and chemical changes in shale that lead to increases, or decreases, in permeability of inter-layers and caprocks, that may mean changes to plume migration behaviour and/or changes to the seal efficiency of caprocks immediately above the $scCO_2$ zone. Hence, it is important to understand these changes to more accurately predict the behaviour of $scCO_2$ plumes within reservoirs. Therefore, the focus of this work will be the changes in mineralogy and structure-transport relationships in shale following $scCO_2$ treatment.

The intention, for carbon sequestration by injection of $scCO_2$, is that the carbon will be entrapped underground over geological timescales similar to those over which methane is naturally trapped in reservoirs. This means that the shale rocks will be in contact with $scCO_2$ over a wide range of timescales. To overcome some of the challenges associated with simulating long timescale processes in lab experiments, heating the shale-$scCO_2$-brine system is used to increase the rates of processes that would otherwise take much longer. In order to predict longer-term geochemical behaviour, it is important to consider different phases of CO_2, and the interaction of shale with carbon dioxide under a variety of conditions of temperature, pressure, and water saturation.

The interactions of CO_2 with Utica Shale, under wet and dry conditions, have been studied (Sanguinito et al., 2018; Goodman et al., 2019, 2020). The minerology of the inorganic fraction of Utica Shale consists of 50% calcite, 20% clays, 15% quartz, and 15% other minerals (Ardakani et al., 2018). Sanguinito et al. (2018) and Goodman et al. (2019) exposed Utica shale samples to dry CO_2. Sanguinito et al. (2018) found the standard BET surface area remained relatively stable following treatment. However, pore size distributions (PSDs) obtained from quenched solid density functional theory (QSDFT), based on a slit/cylindrical pores, found that there was a substantial (compared to BET) decrease in the surface area and volume associated with micropores, but no significant change was seen for mesopores. Non-local density functional theory (NLDFT) analysis of CO_2 adsorption data showed only small changes in pore volume and size distribution of ultra-micropores

following treatment. The apparently conflictual findings suggest the need for more accurate void space descriptors.

Goodman et al. (2019) treated shale samples with either dry $scCO_2$, or a mixture of CO_2 and water. Water acted as a blocking agent between the CO_2 and the sample surface. Interactions were no longer direct, but primarily due to dissolved CO_2 lowering the pH level of the water surface layer. In general, the presence of water acted to exacerbate effects seen previously in Sanguinito et al. (2018). Field-emission scanning electron microscopy (FE-SEM) showed increased signs of etching and pitting in the calcite matrix, with calcite precipitation. Adsorption experiments showed a decreasing trend for the BET surface area, micropore surface area and volume, between approximately 0.9 and 2 nm, with treatment. However, the volume of mesopores increased due to carbonate dissolution.

Goodman et al. (2020) further examined how fluids interact in the natural fractures and matrix pores of Utica Shale. Their results showed pores both opening at the microscale and closing at the nanoscale, depending on their pore type and size classification. They found changes at the micropore scale resulted from carbonate dissolution and precipitation. Analysis of the region between 1000 nm and 15,000 nm, showed porosity increased from 1.8% to 7.6% following treatment with dry CO_2, and by up to 33% following treatment with wet CO_2. This was associated with intraparticle and interparticle pores in the mineral matter and natural fractures as carbonate is dissolved. Pore volumes and PSDs were examined using a combination of CO_2 and N_2 sorption isotherms, and mercury intrusion porosimetry. The surface area (SA) was found to have decreased after treatment in all cases. However, while the outcrop sample SA decreased the most following wet CO_2 treatment, the production sample SA was least when exposed to just CO_2. It was found that different pore size ranges reacted differently during treatment. Carbonate dissolution and precipitation accounted for the opening of the micropores, and this is consistent with the 30% rise in porosity seen in FE-SEM analysis. The decrease in nanopores observed may have been due to aggregation of clay and organic features and precipitating particles. It is generally supposed that minerals will not dissolve in $scCO_2$ (unless at extreme pressure and temperature). However, even small amounts of water dissolved into the CO_2 can initiate reactions, and, also, any water bound on to clay surfaces may have some ability to cause reactions, so these possibilities may be why Goodman et al. (2020) reported that 'dry' CO_2 also led to some reaction.

Yin et al. (2016) studied the longer-term reactivity of $scCO_2$ with Longmaxi shale. This treatment had a limited influence on the mesopores, but more significant impact on the micropores. After treatment, the specific surface area and number of micropores decreased sharply, while the average pore size was enlarged. The fractal dimensions of the shale pore structure decreased after treatment, indicating a decrease in the degree of roughness of the pore surfaces and the morphology of the pore network became smoother. Ao et al. (2017) treated Longmaxi shale with dry CO_2. Using low-pressure nitrogen adsorption data, they reported specific surface area of the shale decreased, and the porosity and average pore size increased. Pores close to 2.32 nm were primarily enlarged. XRD data showed that the content of all minerals except quartz decreased.

To-date, to the authors' knowledge, only one lab-based geochemical experiment has been published on the Sleipner caprock, with Bateman et al. (2013) reporting an investigation to evaluate the impact of CO_2 on the sealing capacity of Utsira caprock. This focused only on dissolved CO_2 interactions as the sample was submerged in porewater prior to CO_2 injection. Several 'batch' experiments were set up, running for up to 5 years. The samples were kept at 30 °C and injected with CO_2 to a pressure of 8 MPa (approximate reservoir conditions). Reactant fluids were regularly sampled for the first 14 months, and again at 5 years, and tested for levels of pH, carbonate/bicarbonate and cations/anions. CO_2 is thought to have reacted with the pore water relatively quickly. pH levels decreased over time, but a slight increase was seen in the final measurement after 5 years. Bateman et al. (2013) comment that this may be due to an increase in pH buffering. A rapid increase in bicarbonate was found. This came directly from CO_2 dissolution, and the dissolution of caprock carbonates caused by the lowering of the pH level. The slowing of bicarbonate increase after the initial burst was said to be due to a decelerating rate of carbonate mineral dissolution. In addition, there was the slow reaction of aluminosilicate minerals which 'consumed' acidity and generated bicarbonate ions as a by-product. Dissolution of caprock sample carbonates was also indicated by the swift increase in calcium and other minor elements in the pore water samples. It was not clear if an equilibrium was reached, or total consumption of the carbonate phase in the sample had occurred. This previous work investigated geochemical changes only, and did not focus on the changes in pore structure or transport properties of the Sleipner caprock, which will be the subject of this work.

In this work, gas overcondensation will be used to probe the interrelationship between large macropores, typically undetected by conventional adsorption experiments, and the rest of the pore size range. The pore-shielding effect in gas desorption allows the probing of surrounding critical pore sizes that control access of a given set of larger pores to the exterior and the determination of pore connectivity (Seaton, 1991). Further, gas sorption scanning will be used to identify key segments of the void space important to mass transport. These void space units can then also be mapped by hybrid gas sorption and imaging methods. The macroscopic (>~μm) spatial distribution of smaller meso- and micro-porosity will be probed in Nordland shale using selective pre-adsorption of an X-ray contrast agent in the smallest pores. This will overcome the issue of the limited fields of view, limiting the statistical representativeness of the results, for FIB-SEM, nano-CT, and 3D-TEM (Arif et al., 2021). In this way, the larger-scale spatial disposition and inter-connectivity of the smallest pores, and the minerals associated with them, will be determined. Complementary CXT imaging of mercury entrapped in macropores alone allows the macroscopic spatial distribution of these pores to be probed independently.

2. Geological background

The geological framework of the Sleipner area, Norwegian sector of the central North Sea (see Figure A1.1(A)), has previously been described by Bøe and Zweigel (2001), and just a summary is presented here. Regionally, the North Sea represents a subsiding basin, filled by alternating units of sands and mudrocks/shales, and in places evaporite units. At Sleipner, the upper Pliocene Nordland Shale provides the seal for CO_2 stored in the underlying Utsira sand (see Figure A1.1(B)). This caprock varies in thickness between approximately 200 m and 300 m in the Sleipner area (Lothe and Zweigel, 1999), and its base is approximately 800 m below sea level.

In the Sleipner area, the sediments of the Nordland shale are typically clay silts or silty clays, and comprise 3 units:

- The Upper Seal, which varies in thickness between 70 and 100 m. Upper Seal sediments largely comprise marine and glacimarine muddy and clayey material, plus some sands, and have been repeatedly influenced by significant glacial episodes (e.g. Graham et al., 2007; Stoker and Bent, 1987; Sejrup et al., 1991).
- Sedimentary units within the Middle Seal are about 100–150 m thick and are generally considered to be fine-grained hemipelagic distal sediments sourced from the large river systems of northern Europe (Gibbard, 1988; Eidvin et al., 2000; Moreau and Huuse, 2014).
- The Lower Seal immediately overlying the storage reservoir (and hence the most important) is some 50–100 m thick, and is mainly composed of shaly, basin-dominated sediment. It also hosts a sand wedge up to 25 m thick. The shale has a high clay content, and drilling logs suggest over 80% shale volume (Chadwick et al., 2002).

The mineralogy of the Nordland Shale shows some variation, but has an average composition of quartz (30%), undifferentiated mica (30%),

kaolinite (14%), K-feldspar (5%), calcite (4%), smectite (4%), albite (2%), chlorite (1%), pyrite (1%), gypsum (1%). Higher in the unit the smectite content is generally low (<4%), but increases at greater depths to reach 9%. The clay mineral content of the <2 μm fraction taken from the lower part of the Lower Seal comprises 41% illite, 37% kaolinite and 23% smectite (Kemp et al., 2001).

Using the classification of Lundegard and Samuels (1980), and on the basis of their silt content (mean c.47%), Kemp et al. (2001) note that their samples can be termed 'mudshales' where laminated or 'mudstones' where massive. Together with the low total organic carbon values (0.68–1.58%), the samples could be further classified as non-organic mudshales and mudstones according to the Krushin (1997) classification.

Kemp et al. (2001) found diagenetic overprinting difficult to assess, however, they noted the following features:

- Some clay particles displayed marginal development of fibrous outgrowths, which may represent authigenic illite, and some more tabular/platey crystals that may be kaolinite/chlorite.
- Framboidal and disseminated pyrite was present in one sample studied.
- There was rare evidence for illitisation of detrital feldspar.

3. Materials and methods

3.1. Materials

Samples for this work were acquired from well 15/9-A11, in the Sleipner field, northern North Sea, from which a 9m core was taken in 2002. This core was positioned in the lower Nordland Shale seal, about 20m above the Utsira sand. Samples were received from the British Geological Survey (BGS) in two forms. Two larger segments measuring 3–4 cm were cut from the edges of borehole sections. An image of an example of such a segment can be seen in Appendix A2. Eight further sample bags were provided containing offcut chips of a mixture of sizes ranging from 2-3 cm to 1 mm. Images of examples of the offcut chips can be found in Appendix A2. All experiments carried out in this work were either using small chips of <1 cm in size, or samples in powdered form. Where chips were needed, a relevant sized chip could be selected from the bags, but a sequence of crushing and sieving was required to create powders of known size ranges.

Using chips and powdered shale samples for mass transport studies eliminates the presence and influence of larger-scale artificial microfractures that may have been induced by coring and transit, and also the impact of stress (Wu et al., 2017). A KHD Humboldt Wedag milling machine was used to crush the larger shale samples into powder. As the shale was very brittle, the machine was only turned on in short bursts for seconds at a time. Care was taken to fully clean the equipment before crushing to reduce the risk of sample contamination. After crushing, the resulting powder contained a variety of grain sizes, and, thus, a sieving process was used to separate the particles into known size ranges. A Sieve Shaker Inclyno 2 manufactured by CAPCO Test Equipment ltd was used to divide the sample into ranges; <53 μm, 53–90 μm, 90–150 μm and >150 μm. The largest grains in the >150 μm sample were <1 mm.

3.2. Treatment of shale with supercritical carbon dioxide

Treatment of shale in laboratory batch reactors would simulate conditions where static CO_2 pools under the caprock or shale interlayers, as occurred in the Sleipner case. Ten different samples of Nordland shale, each of approx. 1g of crushed powder of 150–1000 μm grain size, were treated. Samples were heat sealed into triangular pockets made of 50 μm mesh Nitex nylon filtration fabric. The nylon pockets were suspended inside the stainless steel batch reactors by attachment to a titanium dip tube halfway down the vessel (see Fig. 1a). Four reaction vessels were placed into ovens at 35 °C and 80 °C to equilibrate before pressurising. A schematic of the experimental setup including the four vessels can be seen in Fig. 1b. These two temperatures were chosen to correspond to the minimum geological temperature of the Sleipner caprock (35 °C), and 80 °C to investigate any temperature dependence (Bickle et al., 2007). Higher temperatures should increase reaction rates. Of these four vessels, two were left in a dry condition, and two had distilled water (20 ml) added, with the surface of the water being below the sample. The vessels containing distilled water were magnetically stirred at 200 rpm. The two conditions were compared to determine the effect of moisture content. To remove any air, the vessels were flushed with N_2, followed by flushing with CO_2, and then pressurised with CO_2 up to 90 bar. This pressure corresponds to the median pressure found in the Utsira Formation (Bickle et al., 2007). Two control samples were treated at atmospheric pressure for comparison, one at each aforementioned treatment temperature. Sample treatment times of one week and four weeks were chosen such that comparisons could be made with similar experiments found in the literature (Liu et al., 2012; Kaszuba et al., 2013; Lahann et al., 2013; Mouzakis et al., 2016; Yin et al., 2016; Jedli et al., 2017; Pan et al., 2018). Table 2 shows the sets of treatment parameters for each sample, and the reference number which will be used to refer to each treated sample. It is noted that sample 1848 was destroyed during the treatment process. Following completion of the treatment period, the vessels were slowly depressurised, to prevent extra liquid from splashing onto samples, followed by drying at 35 °C in air, and then samples were individually sealed in plastic bags to protect them until characterisation.

3.3. Gravimetric measurement of total specific pore volume

The gravimetric method used water saturation by vapour phase mass transfer until the pore space was saturated. After pore-space saturation, water could start to condense between grain particles. Care was taken to monitor the calculated volumes as this inter-grain water will give an inflated measurement. The calculated pore volume of the as-received sample was compared to the as-received volume determined using overcondensation data. The time at which these two values were equal, was where all sample volumes were taken as fully saturated. This assumed similar rates of adsorption for all samples.

Samples were degassed in a vacuum overnight at 110 °C to remove any moisture from the atmosphere. The mass of the dry sample was measured before placing in an airtight container supported above a reservoir of deionised water. Sample weights were periodically measured. The first weight was measured after 14 h (overnight), then every 3 h during the day, and then the next day. Once pore-filling had been achieved but before inter-particle filling commenced, the specific pore volumes were calculated from the increase in sample mass from the dry sample using the relevant density of water (0.9982 g/cc).

3.4. Gas sorption and overcondensation

The conventional nitrogen sorption isotherms and rate of adsorption (ROA) data were obtained at 77 K using a Micromeritics 3flex volumetric adsorption apparatus. Equilibration times were set at 30 s unless stated otherwise. Conventional nitrogen isotherms were obtained for all samples listed in Table 1. In each case multiple experiments were run to analyse repeatability. Three powdered as-received shale samples of varying grain sizes were run, as well as a whole chip sample. This allowed investigation of possible pore network changes due to crushing and sieving of the shale. Two chip samples were tested before and after pre-adsorption of iodononane. Adsorption of iodononane was achieved by suspending shale samples above a large reservoir of iodononane, in a sealed container, for 3 weeks at room temperature.

All samples, except the chips containing pre-adsorbed iodononane, were degassed before isotherms were recorded. Empty shale samples were held in a vacuum at 110 °C for 15 h (overnight). Chips containing pre-adsorbed iodononane were not degassed as this would remove the

iodononane from the sample. The aim of iodononane experiment was to record the isotherm with iodononane blocking a proportion of the pores. Moisture from the air should be limited in this case regardless as the samples were degassed before pre-adsorption treatment and were in a sealed container thereafter. For the nitrogen sorption experiments conducted following mercury entrapment and discharge from the porosimeter, the sample was taken directly and rapidly back to 3flex, and frozen by immersion of the sample tube in liquid nitrogen, so that

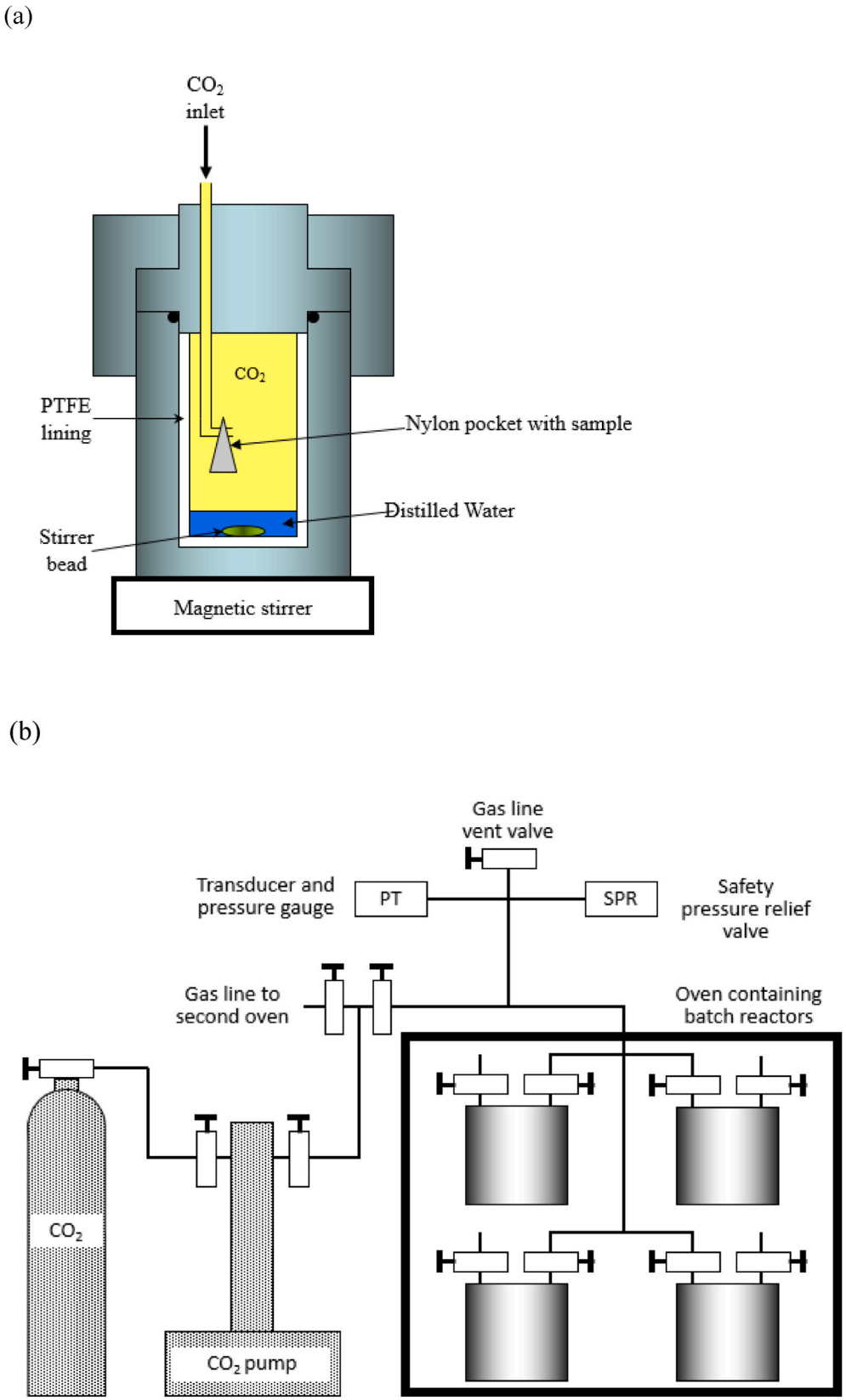

Fig. 1. (a) Diagram of BGS stainless steel batch reactor vessel for $scCO_2$ treatment of samples. (b) Schematic of experimental apparatus for sample treatment, including the four vessels.

Table 1
The sets of treatment parameters for each Nordland shale sample. (DIW = deionised water).

$scCO_2$ treatment					
Run Number	DIW/ mL	Temperature/ °C	Pressure/ bar	Time/ weeks	Sample Weight/g
1845	0	35	90	1	1.003
1846	20	35	90	1	1.001
1847	0	35	90	4	1.001
1848[a]	20	35	90	4	1.002
1849	0	80	90	1	1.001
1850	20	80	90	4	1.001
1851	0	80	90	4	1.000
1852	20	80	90	1	1.000
1853	0	35	Atmospheric	4	1.001
1854	0	80	Atmospheric	4	1.000

Notes.
[a] Sample destroyed.

Table 2
Parameters of the Kloubek (1981) correlation.

	A	*B*	Range of validity (nm)
Intrusion	−302.533	−0.739	6–99.75
Retraction	−68.366	−235.561	4–68.5

mercury extrusion is limited. The sample was left in liquid nitrogen for 20 min before evacuating the sample tube so that the entrapped mercury became solid and would not be evacuated out of the pores. The sample was then left under vacuum overnight to degas.

For the ROA experiments, a single specified pressure/adsorbate dose amount is injected into the sample holder. The rate at which adsorption equilibrium is achieved at this point is measured over time. Uptake on the shale was measured every 0.5 s. The choice of the pressure/adsorbate dose amount for the ROA experiments is important, since uptake needed to be enough to provide sufficient signal-to-noise, but small enough to limit any interference to mass transport from pre-existing adsorbate, such that mass transport parameters are characteristic of empty samples. To find the best pressure dose to use, initial tests were conducted using three different test doses: $P/P_0 = 0.01$, 0.03, or 0.07. After reviewing the data, all further rate of adsorption experiments were run with a pressure dose of $P/P_0 = 0.07$.

Nitrogen overcondensation experiments were performed on a Micromeritics ASAP 2020 physisorption analyser to probe the larger pore sizes and upper end of the hysteresis. The method is based on that of Murray et al. (1999), and is described in detail elsewhere (Rigby et al., 2020a,b).

3.5. Mercury porosimetry

A Micromeritics AutoPore IV 9500 was used for low- and high-pressure mercury intrusion porosimetry. The low- and high-analysis ports take the sample from atmospheric pressure, to under vacuum, and then to 207 MPa (low-pressure) and 414 MPa (high-pressure).

3.6. Mineral liberation analysis-scanning electron microscopy (MLA-SEM)

Four as-received powdered shale samples were tested, each with a different grain size range, namely <45 μm, 45–63 μm, 63–90 μm, and 90–150 μm. This was done to evaluate if the process of crushing and sieving to create these size fractions caused any significate mineral separation. It is important to verify powdered grain sizes are representative of the whole shale, as other experiments use only one powder size range. The treated samples studied were those denoted 1845, 1846, 1847, 1849, 1852, 1853 and 1854.

As sample polishing is more successful closer to the sample/resin interface, powdered samples were used to increase this interface substantially. As-received and treated powder samples of each aforementioned grain size were loaded into individual “beam capsules” and combined with epoxy resin. The samples were left to settle to the bottom of the capsules and then placed into larger resin blocks which could be held by the SEM instrument. Capsules and blocks were then dried in a vacuum oven to remove any air bubbles. Mechanical polishing was then completed using silicon-carbide paper, progressing from 500 to 4000 grit. Changes in the grit amount on the paper was only advanced when all scratches in the surface were uniform under an optical microscope. Between grits the sample was put in a methanol ultrasound bath to clean off removed resin residue. Methanol was again used as the polishing lubricant.

During bombardment by the electron beam, nonconductive samples collect charge and inhibit the emission of secondary electrons. Therefore, the samples were coated in a 10–20 nm layer of carbon to uniformly make the entire surface conductive. Inside the SEM instrument the sample is grounded (earthed) to allow for the dispersion of this charge.

The experiment was carried out using was a FEI Quanta 600 FEG scanning electron microscope, equipped with Bruker high throughput energy dispersive X-ray spectroscopy (EDS) system and backscattered and secondary electron detectors. Instrument conditions and parameters include a high voltage of 20 kV, spot size of 4, and working distance of 12.5 mm. The mineralogy was determined using GXMAP measurement mode within FEI Mineral Liberation Analyzer™ software. Each mineral identified was within an 80% match to a known standard X-ray. Each of these MLA acquisitions took between 3 and 4 h per sample.

Phase segmentation of the minerals and mineral identification by X-ray analysis of the EDS points is completed to produce the MLA results. Grains and mineral fractions within them may be touching therefore a de-agglomeration algorithm was run to separate these phases. The contrast in grey-scale backscattered electron imaging was used to achieve this. Heavier element minerals are brighter, lighter elements are darker. EDS at each point assigns a colour for each mineral identified, producing a map of the sample and modal mineralogy by area.

3.7. Computerised X-ray tomography

High Resolution X-ray 3D Computed Tomography imaging was carried out using a GE Phoenix Nanotom® XCT System. The scanner was set at 90 kV electron acceleration energy and 105 μA current, with the detector set at a distance of 200 mm. The shale chips were 10 mm from the X-ray source with 0.1 mm copper filter. A total of 1800 projection images were collected using a detector exposure of 750 ms integrated over 5 averaged images resulting in a scan time of 112.5 min. The resulting image resolution obtained was a voxel size of 2.5 μm. The settings were held constant for each scan.

The micropore mapping with CXT will also be used to enhance interpretation of complementary interventionist studies of the mass transport utility of micropores in as-received shale by simultaneously using the CXT contrast medium, additionally, as a selective pore-blocking agent to ‘filter-out’ the micropores from the network (Hill--Casey et al., 2021). This physical segmentation of the accessible void space avoids some of the problems with proper accounting of void space features in corresponding imaging approaches susceptible to missing out pores due to detection, sampling, or gating issues (Arif et al., 2021). Some studies have imaged liquid-phase, molecular diffusion in shales with CXT, since then the density of the probe fluid is high enough for X-ray absorbance to be detectable (Zhang et al., 2018, 2019). However, gas phase diffusion may sample the void space differently because of differences in the resistance distribution between molecular and Knudsen regimes due to their different pore size dependence. While CXT can determine if the diffusive flux of contrast agent enters particular solid phases, based on X-ray absorbance, it cannot tell through which

particular pore sizes the flux mainly permeates a given phase. In this work, using the aforementioned filtering strategy, the relative importance, to gas-phase mass transport, of the smaller micropores and mesopores below CXT resolution will be assessed.

4. Theory

4.1. Gas sorption

Rocks are complex mixtures of different minerals. The homotattic (meaning isoenergetic) patch model was introduced in order to account for the impact on adsorption of the chemical heterogeneity of such surfaces (Walker and Zettlemoyer, 1948). This model considers the surface of the adsorbent to consist of a patchwork of different types of site, perhaps corresponding to different mineral grains, each with their own characteristic adsorption behaviour. The model assumes that each of these patches is large, such that edge effects, where they neighbour other patches, are negligible. The resulting overall adsorption is thus a composite of the behaviour of the set of patches, such that:

$$V = V_m(\theta_1 I_1 + \theta_2 I_2 + \ldots + \theta_i I_i + \ldots), \tag{1}$$

where I_i is the isotherm equation describing adsorption on the ith patch, and θ_i is the fraction of the surface occupied by patches of type I_i, such that the various θ_i-values obey:

$$\theta_1 + \theta_2 + \ldots + \theta_i + \ldots = 1. \tag{2}$$

Much previous work utilising the homotattic patch model has only characterised each surface patch by an adsorption energy and used the model to simply *a posteriori* curve-fit experimental adsorption isotherms without using the fitted parameters to make any predictions regarding other physical properties of the system. For example, Ng et al. (2017) only fitted Langmuir-type isotherm models, that only have monolayer capacity and adsorption energy parameters, even into the multilayer and capillary condensation regions of the isotherms fitted. However, the surfaces within different patches may have additional properties besides just adsorbate interaction strength that can be probed by adsorption isotherms.

Natural rock surfaces are often rough at a molecular scale. This roughness is neglected in conventional models of gas sorption, such as the standard Brunauer-Emmett-Teller (BET) equation (Rouquerol et al., 1999). Concavities in the surface mean that the space for adsorbing the second and subsequent layers of an adsorption multi-layer declines with distance from the surface, and the maximum molecular capacity of each successive layer decreases. For surfaces that exhibit the particular property of self-similarity over several length-scales, and are, thus, fractals, the decrease in the capacity of each layer of adsorbate is given by the equation (Avnir and Farin, 1984):

$$\frac{A_i}{A_1} = i^{2-d} \tag{3}$$

where A_1 is the area in the first adsorbed layer, A_i is the area in the ith adsorbed layer, and d is the surface fractal dimension ($2 \leq d \leq 3$). This effect can be incorporated into the standard BET model such that a fractal version thereof is obtained. This is given by (Mahnke and Mögel, 2003):

$$log(v) = log(v_m) + log\left[\frac{cx}{1 - x + cx}\right] - (3 - d)log(1 - x), \tag{4}$$

where v is the amount adsorbed, v_m is the monolayer capacity, c is the BET constant, and x is the relative pressure. The effect of the fractal roughness, as described by Equation (3), is to lead to a decline in the amount adsorbed in each successive layer of adsorbate thereby making the upper parts of the adsorption isotherm sensitive to differences in surface roughness. Hence, in the homotattic patch model, the nature of the patches can be characterised by both the surface adsorption energy and its geometric roughness. Different parts of an adsorption isotherm are sensitive to these two aspects, with the low pressure, monolayer region sensitive to the interaction strength (surface chemistry), and the higher pressure multi-layer region sensitive to the roughness, such that these characteristics can be probed independently by adsorption alone. In this work, it will be tested whether the multilayer region can be used in this way, and that the homotattic patch model does not just give rise to adjustable parameters in an empirical curve-fit, but to physically meaningful properties that are further predictive of other physical processes, namely mass transport. The homotattic patch model also offers an alternative approach to CXT with which to associate changes in mass transport flux to the appearance of particular types of pores, such as those surfaced with organic matter (Pitcher et al., 2021).

4.2. Gas uptake kinetics

Mass transport properties can be characterised by kinetic gas uptake experiments. Kinetic mass uptake data, comprising amount adsorbed versus time, typically takes the mathematical form of an exponential growth, and, thus, is often fitted to the so-called Linear Driving Force (LDF) model. The characteristic parameter of this process is the mass transfer coefficient, denoted k. The LDF k-value is defined by the function (Rigby, 2020):

$$M = M_0\left(1 - e^{-kt}\right) \tag{5}$$

where M the amount of nitrogen adsorbed at time t, M_0 is the ultimate total adsorbed amount of nitrogen for the adsorption pressure point, and k is the mass transfer coefficient. The apparent mass transfer coefficient, obtained from a fit to raw uptake data, must be corrected for the effect of concurrent adsorption using the slope of the isotherm at the relevant adsorption pressure point. In this way the actual mass transfer coefficient is obtained.

For a porous sample, the mass transfer coefficient k depends upon the intrinsic effective diffusivity of the pore network D, the diffusion penetration depth a, and a geometric factor, which is 15 for a spherical particle (Rigby, 2020):

$$k = \frac{15D}{a^2}. \tag{6}$$

When a pore structure is modified this can be manifested in a change in D, or a, or both. For example, a loss of pore connectivity would result in an increase in network tortuosity, and, thence, a decline in network diffusivity, and a decrease in observed k-value. However, the blocking of external diffusive access to the core of a particle would result in a drop in the penetration depth a, and thus a rise in the observed k-value. Hence, if a vital percolation path connection within the pore network is lost then the mass transport is curtailed.

In a kinetic uptake experiment there may be some overlap in the timescales over which concentration equalisation happens in the sample chamber and uptake occurs into the sample, and samples may be heterogeneous materials with different phases or regions which have different uptake rates. In which case a multi-component LDF model can be fitted to the raw mass uptake curves:

$$M = (\theta_1 M_1 + \theta_2 M_2 + \ldots + \theta_i M_i + \ldots) \tag{7}$$

where θ_i is the fraction of component i, and all values of θ_I sum to unity, as in eq. (2).

4.3. Mercury porosimetry

In this work mercury entrapment will be used to selectively highlight the spatial distribution of the largest pores in the network using CXT. In order to demonstrate which particular pores the mercury becomes entrapped within, it is necessary to be able to remove contact angle hysteresis from the raw porosimetry data thereby revealing for which

pores mercury intrusion is reversible. This can be achieved using a semi-empirical modification of the Washburn (1921) equation calibrated using porosimetry data for a structurally-regular material, namely controlled pore glass, where the pore size can be independently determined from electron microscopy (Liabastre and Orr, 1978).

The so-called Washburn (1921) equation typically used to analyse mercury porosimetry data is given by:

$$p = \frac{-2\gamma \cos \varphi}{r}, \tag{8}$$

where p is the imposed pressure, γ is the surface tension, φ is the contact angle, and r is the pore radius. Kloubek (1981) utilised the calibration data of Liabastre and Orr (1978) to establish the relationships for the variation of the product $\gamma.cos\varphi$ as a function of pore radius, for both advancing and retreating mercury menisci, even for nanopores. Kloubek (1981) obtained expressions of the form:

$$\gamma \cos \varphi = A + \frac{B}{r}, \tag{8}$$

where A and B are constants whose values are dependent on whether the mercury meniscus is advancing or retreating. The values of these constants found for the CPGs, and their pore size ranges of application, are given in Table 2. However, the form of the correlation has been successful for other materials too, and alternative values of the parameters

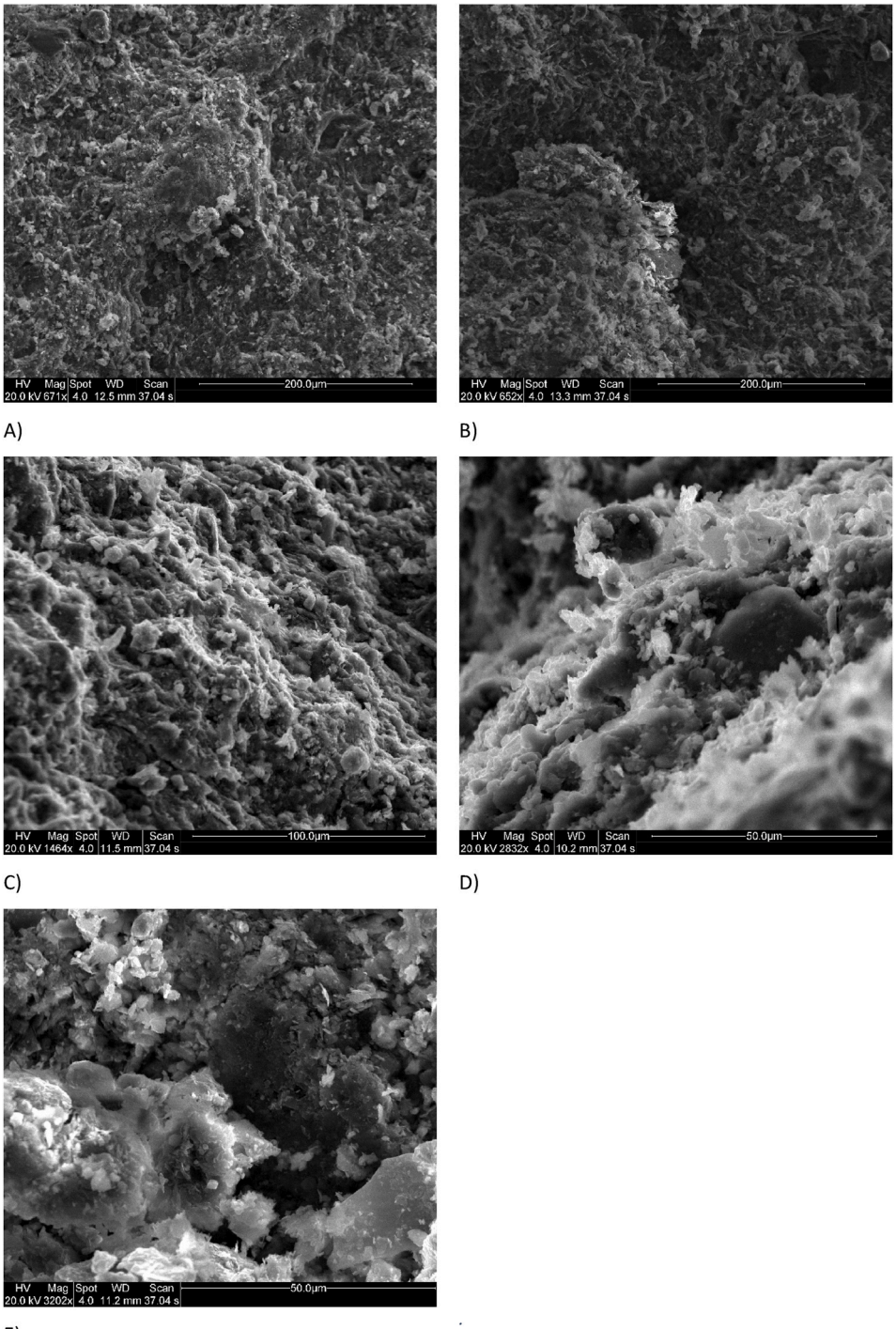

Fig. 2. Secondary electron SEM imaging of as-received whole shale chips showing general surface features.

A and *B* have been found for these other materials (Rigby, 2000).

5. Results

5.1. MLA-SEM

Fig. 2 shows secondary electron (SE) images of the as-received, unpolished shale chips at three different magnifications. SEs originate from, and so image, the surface or near-surface region of the sample. The brightness of the signal depends on the number of secondary electrons reaching the detector. Steep surfaces and edges tend to be brighter than flat surfaces producing a well-defined three-dimensional appearance. The images reveal a highly irregular surface with roughness over length-scales ranging from hundreds to a few microns. The attempt to polish a flat surface of these chips was unsuccessful, therefore MLA was not possible.

However, the semi-polished finish did allow for limited EDS on selected minerals. Imaging on this surface also highlighted the source of some of the void space in the shale. Fig. 3 shows an example of this imaging and the EDS response. The green cross is the point under inspection which produced the spectrum in Fig. 3B. The elemental results were matched to kaolinite in this case. However, in addition, titanite, illite, ilmenite, smectite-type clays, muscovite, orthoclase, apatite, zircon, pyrite and calcite were also identified in this way. The subjective sampling of this method does not give a statistically representative overview of the shale minerology.

Classification schemes for mudrock pores typically include three major matrix-related pores types (Loucks et al., 2012). Two of these types related to the mineral matrix, and consist of interparticle and intraparticle pores, while the third type is the intraparticle pores located within organic matter. Using this classification technique, the semi-polished SEM images, given in Fig. 4, show a variety of mineral matrix inter- and intra-particle pores. Large interparticle macropores can be seen in Fig. 4B, where the majority of this pore type surround rigid grains such as quartz, feldspar and pyrite. The shale samples are from a relatively shallow core drilled at about 700m. As suggested by Loucks et al. (2012), interparticle pores are common in shallow sediments but reduce in abundance by compaction and cementation over time and with increased depth. In mudrocks, the size of interparticle pores is generally around 1 μm, but this can range from 50 nm to several microns (Loucks et al., 2012). This is similar to the size range of the visible interparticle pores seen here. Several intraparticle pores are also seen in the imaging data. These pores are only visible at the higher magnifications found in Fig. 4D–F. Cleave-sheet intraparticle pores within the illite/mica clay are highlighted in Fig. 4D, and intra-crystalline pores within the bright pyrite framboids can be seen in Fig. 4F. Similar features are common to many of the shales (Loucks et al., 2012).

While it was not possible to obtain the modal mineralogy of the chip samples, MLA was completed on powdered as-received samples for four different grain size ranges. The results of the scans after mineral phase segmentation and identification can be found in Appendix 3. From these images the modal mineralogy could be calculated for each sample. Due to a possible size selection effect for minerals during sieving, discussed in Appendix 3, the majority of the analysis in the work is performed on the samples with the largest particle size (>150 μm-1 mm).

Fig. 5 shows the modal mineralogy for the as-received and treated shale samples. It can be seen that there is a clear relative decrease in biotite, albite and smectite following treatment, and, thus, a concomitant relative increase in illite. This suggests that treatment has led to the modification or dissolution of biotite, albite and smectite. FTIR spectra for the as-received shale, and for shale after treatment under sets of conditions 1851 and 1852, were also obtained and are shown in Appendix 4. These data suggested that carboxylic acid groups had been added to the shale as a result of treatment.

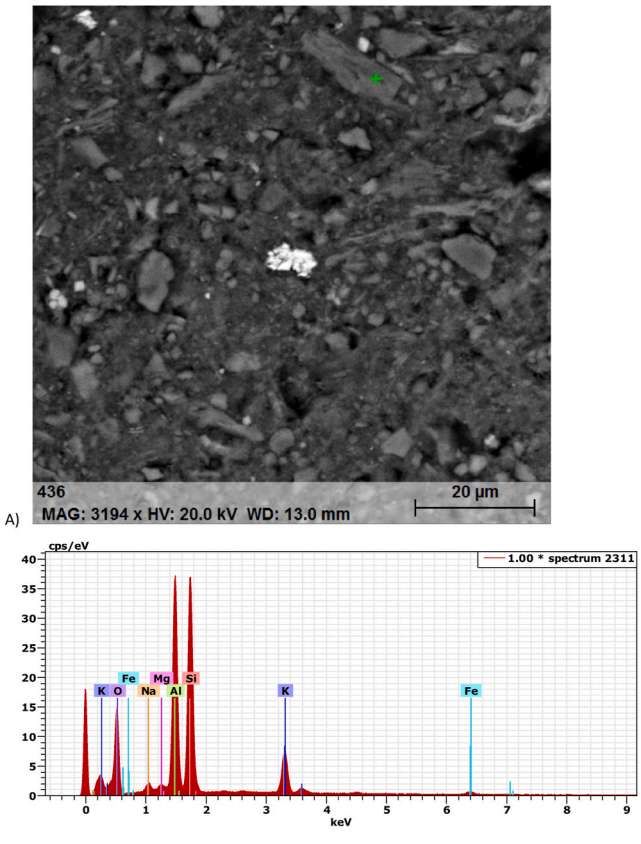

Fig. 3. Example of (A) semi-polished surface SEM imaging of as-received shale chip; and (B) EDS results from the location indicated by the green cross in the image. The spectrum matches kaolinite in this case. (For interpretation of the references to colour in this figure legend, the reader is referred to the Web version of this article.)

5.2. Gas adsorption

5.2.1. Impact of thermochemical treatment on nitrogen adsorption isotherms

Given that shale rocks are very heterogeneous, it was important to assess the level of inter-sample variability in the gas sorption data for as-received shale material before comparing with corresponding data for treated samples. Nitrogen sorption isotherms were obtained for a total of 19 samples of as-received shale, and these data are shown in Appendix 5. It was found that the confidence interval was a narrow range around the mean, and thus the isotherms are closely repeatable.

Fig. 6 shows the individual sample mean isotherms for the samples of repeated isotherms for treated shale batches compared to the sample mean isotherm for the as-received shale (as shown in Appendix 5). In each case, for each batch of treated shale, the sample mean, from multiple runs, and the 95% confidence level on the mean, are depicted. In each case, it can be seen that the 95% confidence level regions for the as-received and treated samples do not overlap at all for relative pressures below ~0.8. These comparisons show that the changes in nitrogen adsorption following treatment are statistically significant. In general, a tighter confidence level is found under about 0.8 relative pressure before widening as the data approaches saturation pressure. This is due to the increase in variability seen in the conventional adsorption data close to relative pressure of unity due to the increasing limitations on the precision of the relative pressure that the apparatus used can achieve.

5.2.2. Modelling of conventional nitrogen adsorption isotherms

The nitrogen adsorption isotherms for powder shale samples with particle sizes >150 μm were fitted to the standard BET model using the

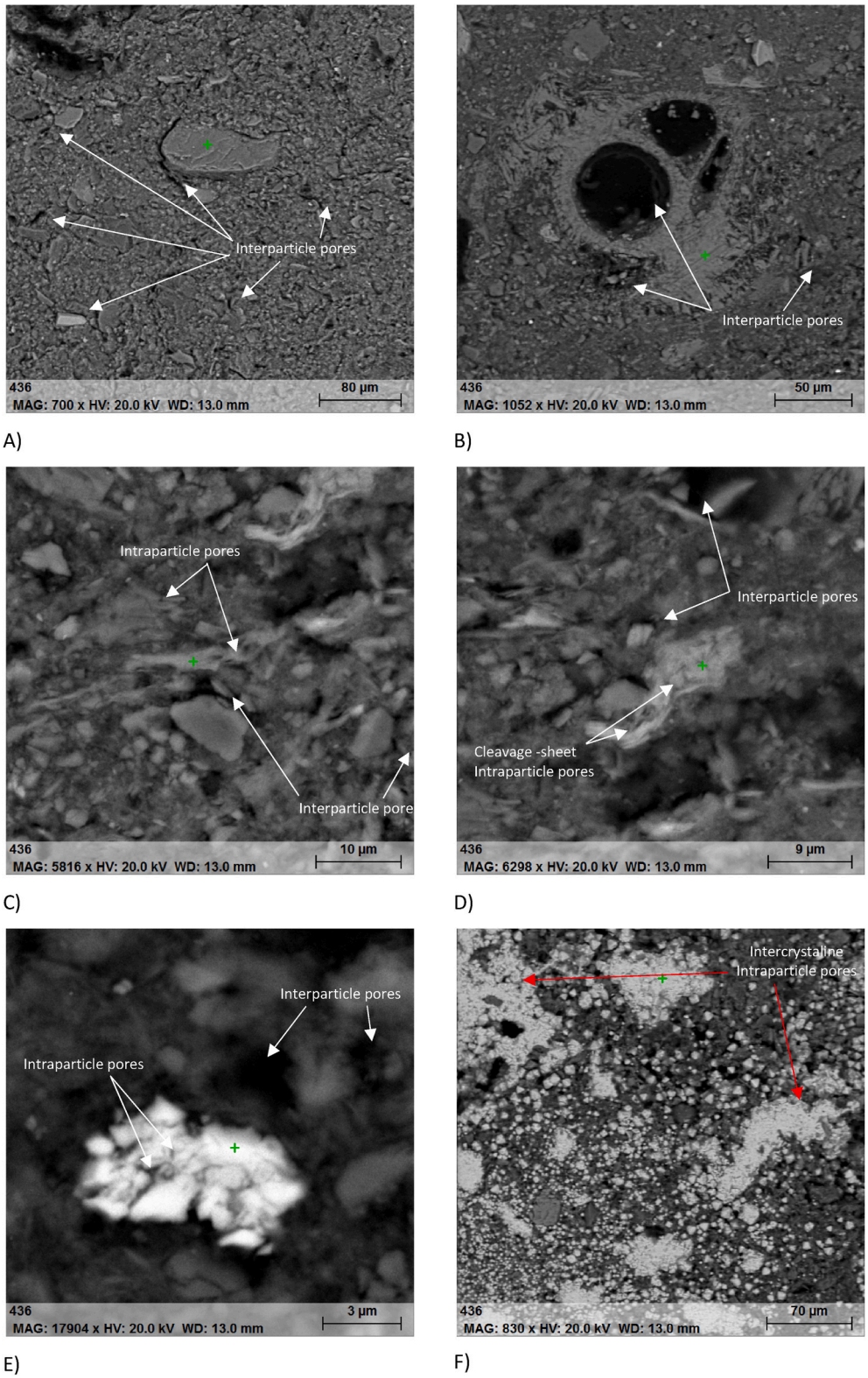

Fig. 4. SEM images of semi-polished surfaces of as-received shale chip samples. Annotations highlight inter- and intraparticle pores in the mineral matrix.

International Standards Organisation, (2010) method, and the results for surface area are given in Appendix 5. The relative differences in BET surface area between the treated samples and the as-received samples are shown in Fig. 7. Most of the treated samples showed decreases in surface area (1845, 1847, 1849, 1851, 1853 and 1854), but the three samples which were treated with 20 ml of deionised water in addition to the $scCO_2$ all showed increases in surface area (1846, 1850 and 1852). The surface areas for samples 1850 and 1852 increased more than that for sample 1846, which may be due to the higher temperature (80 °C) used during the treatment of these two samples. These increases in surface area for Nordland contrast with the finding of decreases for Utica (Goodman et al., 2019, 2020) and Longmaxi (Yin et al., 2016) shales.

Examples of the fits of the standard BET isotherm using the ISO (2010) method are shown in Fig. 8. As can be seen from Fig. 8, the

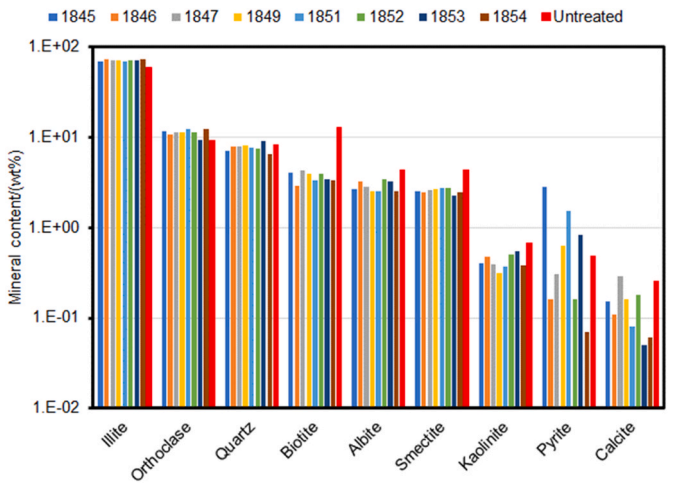

Fig. 5. Mineral composition of treated powder samples of shale (sample numbers as given in Table 1), and of a powdered as-received sample as a reference.

standard BET equation only fits the experimental data over a very limited range when extrapolated beyond the standard range suggested by the ISO (2010). Therefore, the nitrogen adsorption isotherms for as-received and treated samples were also fitted to various types of homotattic patch models. The types of isotherm model considered are shown in Table 3.

Each type of model in Table 3 was fitted to the data for the as-received and treated shale samples. All of the isotherm model types mentioned in Table 3 only include van der Waals force modelling of multi-layer adsorption, and neglect surface tension and capillary condensation effects. Therefore, these models must always predict lower amounts adsorbed than is actually observed once capillary condensation commences. Hence, the range of the fit for these models should be restricted to the lowest relative pressures as possible to avoid fitting regions with contributions from capillary condensation effects. The initial selection of the most appropriate model was based on certain key criteria:

1. The statistical quality of the fit;
2. The lack of overprediction of amount adsorbed for relative pressures above the fitted range;

Examples of the fits of the models in Table 3 to typical adsorption data for an as-received shale sample are shown in Fig. 8. The fits shown were fitted to data over the relative pressure range $0 \leq P/P_0 \leq 0.7$. It was found that for as-received samples that models 1, 2, 5 and 6 over-predicted the amount adsorbed at high relative pressures even when the fitting range was extended up to a relative pressure of 0.7. These models were thus considered inappropriate. Further, according to the criteria given above, it was found that models 3 and 4 had a poorer fit than models 7 and 8 at low pressures, as seen in the logarithmic plot in Fig. 8. Overall, model 8 (2 fractal BET + Henry's Law) was selected as the best model (in terms of statistical quality of fit) for the as-received shale samples. Similar results (not shown) were found for the treated shale samples. The parameters obtained from the fits of the data over the relative pressure range $0 \leq P/P_0 \leq 0.7$ to Model 8 are shown in Table 4.

From the fitted parameters in Table 4, it can be seen that the distribution of the three patch weightings (θ_1, θ_2, θ_3) are largely similar for each sample. The Henry's Law patch is the most abundant at 44–54% of the surface, and the two fractal BET patches are largely similar in size to each other at 20–30% of the surface. The Henry's Law patch has lower interaction constant (B) values compared to either of the fractal BET patch constants (c_1 or c_2). Since these constants are related to the heat of adsorption, this suggests that while Henry's Law patches make up half of the sample surface, they have the least adsorption affinity. The magnitudes of the interaction parameter for patch-2 (second fractal BET component) are considerably larger than the patch-1 (first fractal BET component) constants, meaning the nitrogen adsorbate will preferentially adsorb to patch-2. Compared to all other samples, sample 1851 has the lowest magnitude patch constants (either for fractal BET or Henry's Law), and the lowest surface area.

From the data in Table 4, there is a clear correlation between the addition of deionised water (DIW) when treating the samples with $scCO_2$, and an increase in surface fractal dimension relative to the as-received sample. This is also true of the surface area values. For the shale samples treated without added water present, increased treatment time accentuates the trends for fractal dimension of patch 1 and surface area. In particular, for samples held at 35 °C, the fractal dimension of patch 1 starts at 2.54 for as-received samples, then decreases to 2.42 after 1 week treatment, and then reduces further to 2.17 after 4 weeks. For samples held at 80 °C the corresponding series in fractal dimensions is 2.54, 2.47, 2.34 for as-received, 1 week and 4 weeks treated samples, respectively. The total sample surface area also decreases further with increased treatment time when added water is not present. These trends in fractal dimension and surface area for samples without added water are in line with those observed for Longmaxi shale (Yin et al., 2016).

The changes in the total homotattic surface area with thermochemical treatment are compared with the corresponding changes in the ISO BET surface area in Fig. 7. From Fig. 7, it can be seen that the two surface area methods show some differences in their estimates of the size and direction of these changes. The changes in ISO BET surface area and total homotattic patch model surface area for the various thermochemical treatment conditions were correlated with the changes in mineral composition from MLA (shown in Fig. 5). It was found that the changes in both total specific surface area measures showed a statistically significant correlation ($p < 0.05$) with regression against just the change in the plagioclase feldspar (albite) content, but not for multiple linear regression (MLR) with the changes for all three minerals showing significant decline following treatment in Fig. 5, although the coefficient of determination then for both was 87%.

5.2.3. Nitrogen sorption scanning curves

This section shows how nitrogen scanning curves can be used to demonstrate that the conventional raw isotherm data is really a composite, that can be deconvolved into the contributions from the underlying sub-networks within the shale void space. Fig. 9 shows the conventional nitrogen desorption isotherm and descending scanning curves starting at ultimate relative pressures of 0.95 and 0.93 on the adsorption boundary isotherm for the as-received shale samples, of particle sizes >150 μm. The equivalent data for $scCO_2$ treated samples 1851 and 1852 (without and with water, respectively) are shown in Appendix 6. It was found, in all cases tested, that the desorption for the scanning curves starting at relative pressures of 0.95 and 0.93 commences immediately upon reversing the direction of the pressure change, and all the desorption branches descend and cross the hysteresis region to all converge at a relative pressure of ~0.8.

Fig. 10 shows nitrogen sorption descending scanning curves starting at an ultimate relative pressure of 0.82 on the adsorption boundary isotherm for the as-received shale samples, of particle sizes >150 μm. Equivalent data for treated samples 1851 and 1852 are shown in Appendix 6. As with the descending scanning curves starting at higher relative pressure, in all cases tested, the desorption commences immediately upon reversing the direction of the pressure change. However, while the descending, desorption branches gradually cross the hysteresis loop region, they only get about half-way before deviating dramatically to converge with the lower hysteresis closure point.

Fig. 11 shows nitrogen sorption ascending scanning curves springing from an ultimate relative pressure of 0.8 on the conventional desorption boundary isotherm for the as-received, shale sample, of particle sizes >150 μm. Equivalent data for treated samples 1851 and 1852 are shown

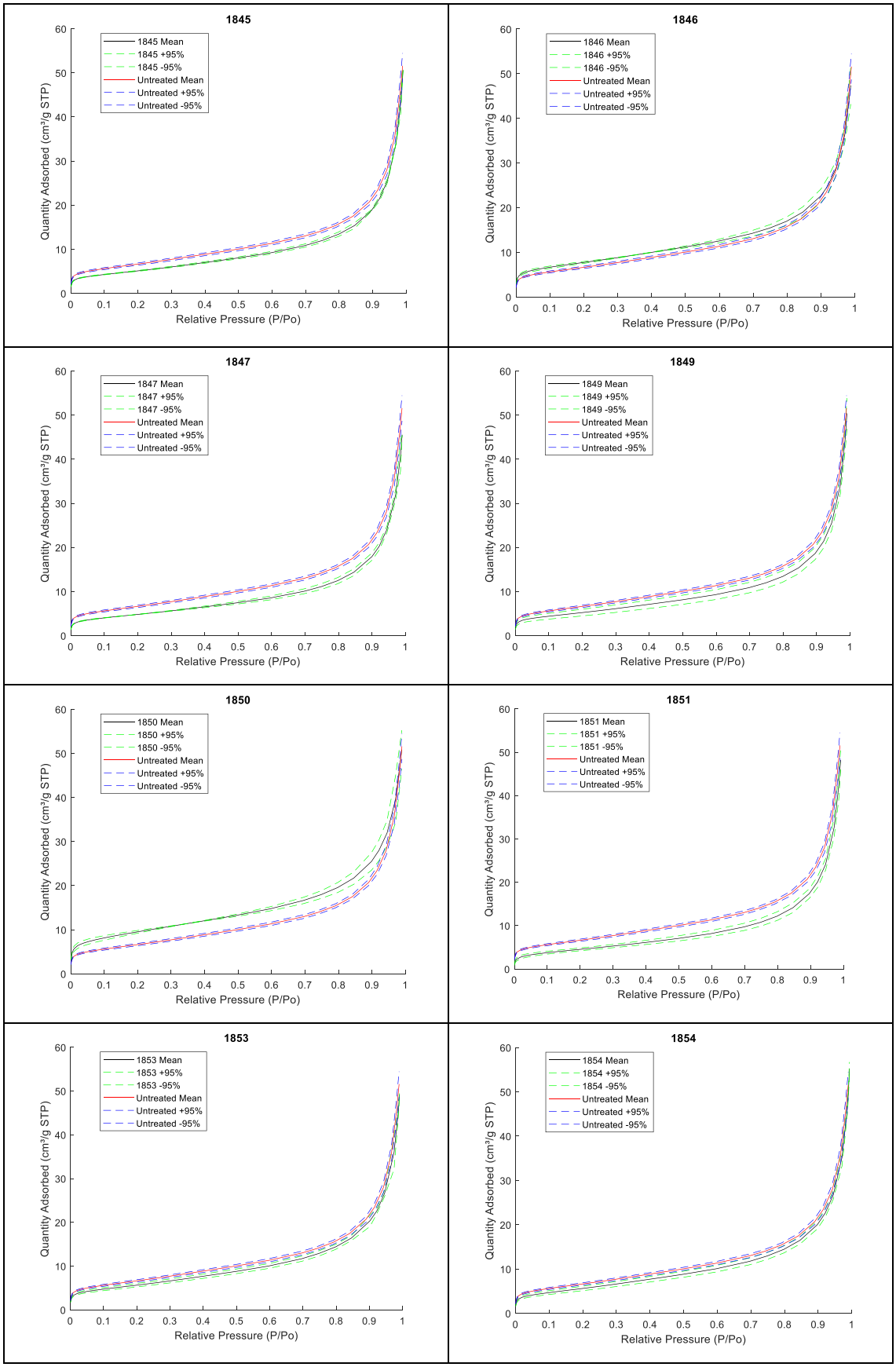

Fig. 6. Comparison of sample mean nitrogen adsorption isotherm (red solid line) for as-received shale with corresponding sample mean isotherms for various treated samples indicated by their sample number. Also shown, for both treated and as-received sample data, are the 95% confidence interval lines (dashed lines) for the corresponding sample mean isotherms. (For interpretation of the references to colour in this figure legend, the reader is referred to the Web version of this article.)

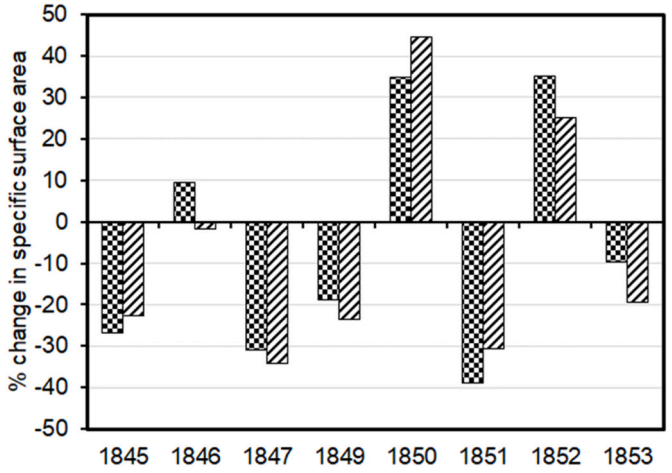

Fig. 7. Percentage change, for treated shale samples, in ISO BET surface area (checkerboard pattern), and 3-component (two fractal BET and Henry's law) homotattic patch model surface area (diagonal shading), relative to the corresponding value for as-received >150 μm powder.

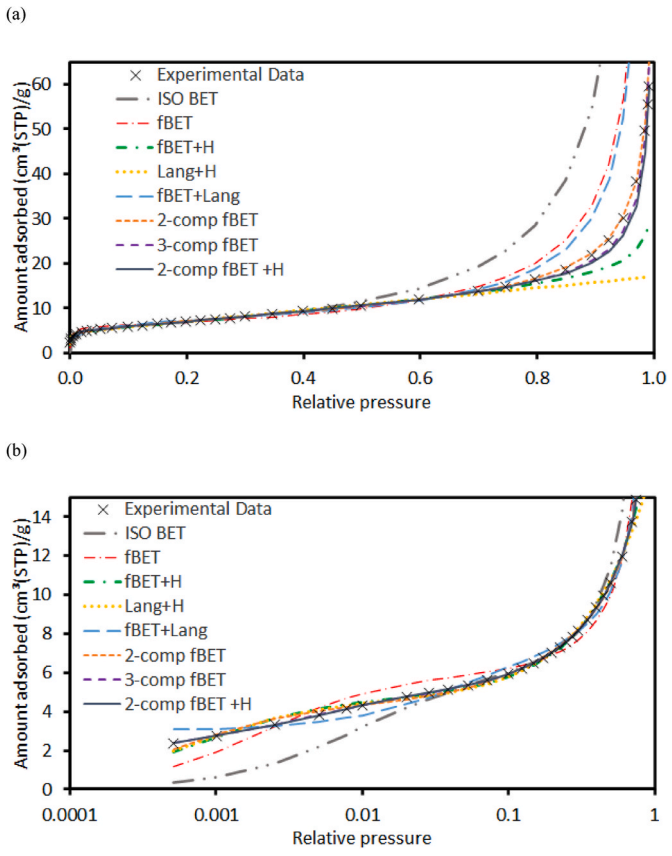

Fig. 8. Nitrogen adsorption isotherm for >150 μm as-received shale sample (×) on linear (a) and semi-log (b) co-ordinates. Also shown are fits of these data to eight different isotherm models, which have been fitted to the data over the relative pressure range $0 \leq P/P_0 \leq 0.7$. (fBET = fractal BET; H = Henry's law; Lang = Langmuir; comp = component).

in Appendix 6. In all cases tested the ascending scanning curves are quite flat, since they cross the hysteresis loop region with relatively little increase in amount adsorbed, and reach the boundary adsorption isotherm at a relative pressure of ~0.92.

The nitrogen sorption scanning curves suggest that the void space of the shale can be considered a composite of two thermodynamically-independent networks, denoted 1 and 2, in order of increasing pore sizes. This is because, while the desorption scanning curves initiated from the adsorption boundary curve at relative pressure around 0.8 are converging on the lower hysteresis closure point, those initiated further up the isotherm at relative pressures higher than 0.8 converge instead on a point on the boundary desorption isotherm at a relative pressure of 0.8. This latter result suggests a concealed lower hysteresis closure point for a network of larger pores, namely Network 2. The ascending scanning curves initiated at this upper convergence point are crossing. This form suggests they may be like the top flat plateau of the hysteresis loop for a network containing smaller mesopores, namely Network 1, filling completely below relative pressures of ~0.8. The slight rise in the crossing, ascending scanning curve is due to multi-layer adsorption occurring in the emptied larger mesopores and macropores of Network 2. The overall forms of the scanning curves are, thus, consistent with the overall observed hysteresis loop region of the isotherm being a composite of two separate isotherms. The first is due to adsorption in smaller mesopores that fill below relative pressures of ~0.8, and the second is due to adsorption in larger mesopores and macropores that experience capillary condensation above relative pressures ~0.8. The similarity of the scanning curve forms for treated and untreated samples suggests thermochemical treatment does not break down the distinction between Networks 1 and 2.

Table 3
Types of isotherm model considered for shale data.

Model number	Number of isotherm components	Component isotherms
1	1	ISO BET
2	1	Fractal BET
3	2	Fractal BET + Henry's Law
4	2	Langmuir + Henry's Law
5	2	Fractal BET + Langmuir
6	2	Two fractal BET
7	3	Three fractal BET
8	3	Two fractal BET + Henry's Law

It has been seen in the scanning curve isotherm data that Network 1 is associated with capillary condensation up to a relative pressures of 0.8. The Barret-Joyner-Halenda (BJH) (Barrett et al., 1951) method was used to calculate a PSD for the shale samples. The particular pore volumes for Network 1 in each shale sample were extracted from the BJH PSD from the adsorption branch, and this corresponds to pore sizes up to 10.7 nm. These volumes are given in Appendix 6. The relative changes in Network 1 pore volume for treated shales, compared to untreated, are shown in Fig. 12. It is noted that the positive changes are associated with shale samples whose thermochemical treatment conditions included added water. Multiple linear regression (MLR) analysis, of the changes in mineral composition with the changes in pore volume of Network 1 following thermochemical treatment (shown in Fig. 12), was found to give rise to a statistically-significant correlation ($F = 11.89$, $p = 0.0207$) for the combined plagioclase feldspar (albite) and smectite clay components (see Fig. 5).

5.2.4. Nitrogen overcondensation and gravimetric measurement of total pore volume

Fig. 13 shows a comparison of the upper parts of the overcondensation boundary desorption curves with the conventional nitrogen sorption isotherms for the as-received and 1850 shale samples, of particle sizes >150 μm. The vertical drop in the overcondensation data at a relative pressure of ~1 corresponds to the evaporation of the bulk condensate outside the sample. The sharp knee thereafter, followed by a (short) plateau corresponds to the state of pore-filling of the shale samples with condensate. It can be seen that, in both cases shown in Fig. 13, this knee and plateau arise at amounts adsorbed substantially higher than the ultimate adsorption obtained in the conventional experiment (up to a relative pressure ~0.995). It can also be seen that, in

Table 4
Parameters of 3-component (two fractal BET and Henry's law) homotattic patch model 8 obtained from sample means for fits of nitrogen adsorption isotherms for as-received and treated shale samples. The subscripts on the parameters refer to component number. DIW = deionised water. The adjusted r^2 is the typical value for a single fit.

Treatment pressure		90 bar							Atmospheric	
Treatment temperature/°C		35			80				35	80
Treatment period/weeks		1		4	1	4		1	4	
Use of water		None	DIW	None	None	DIW	None	DIW	None	None
Sample	As-received	1845	1846	1847	1849	1850	1851	1852	1853	1854
v_m	10.3	7.93	10.1	6.76	7.84	14.82	7.11	12.83	8.26	8.25
θ_1	0.24	0.28	0.29	0.26	0.27	0.26	0.24	0.31	0.27	0.27
θ_2	0.25	0.23	0.28	0.24	0.27	0.22	0.20	0.24	0.27	0.26
θ_3	0.51	0.49	0.43	0.50	0.46	0.52	0.56	0.45	0.46	0.48
c_1	203.63	204.21	196.37	144.82	188.87	161.19	59.92	199.98	191.75	196.69
c_2	9541.91	11193.77	6064.39	5937.46	8726.02	5611.55	2674.49	9239.91	8816.42	9069.14
d_1	2.54	2.42	2.78	2.17	2.47	3.00	2.34	2.94	2.51	2.53
d_2	2.55	2.39	2.56	3.00	2.48	3.00	3.00	3.00	2.45	2.47
B	1.43	1.39	1.83	1.63	1.63	1.62	1.29	2.19	1.74	1.82
Surface area/(m^2/g)	44.91	34.72	44.18	29.63	34.35	64.91	31.15	56.18	36.19	36.14
Adjusted R^2 (%)	99.992	99.976	99.984	99.989	99.988	99.976	99.987	99.986	99.989	99.992

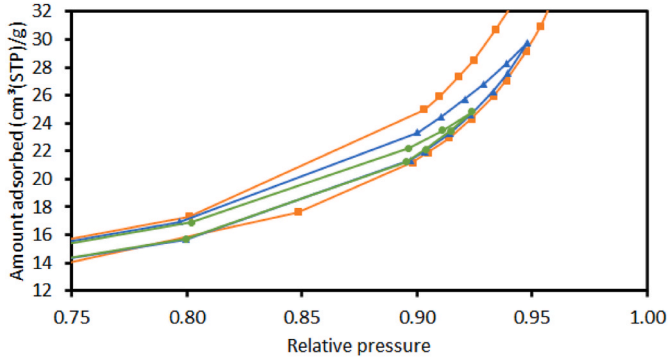

Fig. 9. Nitrogen sorption isotherms with desorption starting at ultimate relative pressures of 0.99 (■), 0.95(▲) and 0.93 (●) on the adsorption boundary isotherm for the as-received shale sample, of particle sizes >150 μm.

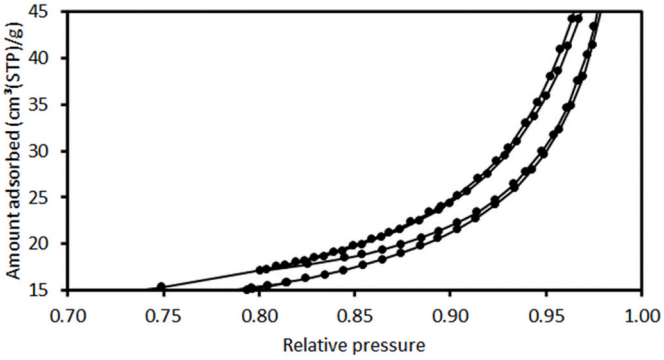

Fig. 11. Nitrogen sorption ascending scanning curves springing from an ultimate relative pressure of 0.8 on the conventional desorption boundary isotherm for the as-received shale sample, of particle sizes >150 μm.

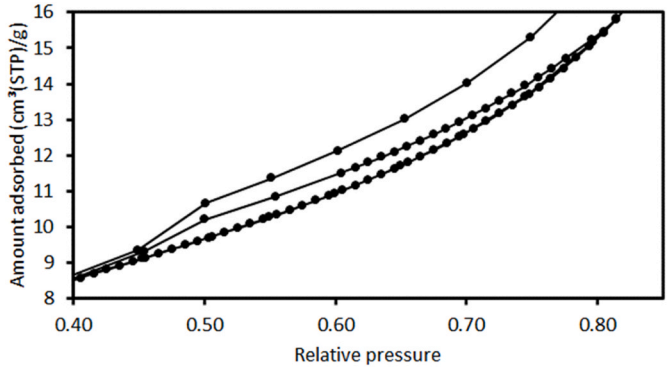

Fig. 10. Nitrogen sorption descending scanning curves starting at an ultimate relative pressure of 0.82 on the adsorption boundary isotherm for the as-received shale sample, of particle sizes >150 μm.

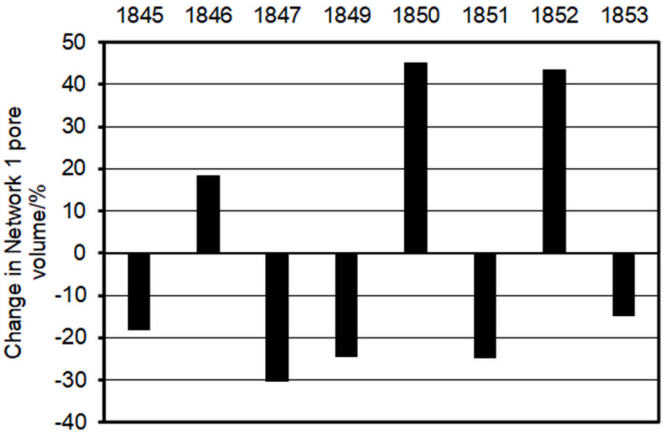

Fig. 12. Changes in pore volume for Network 1 (pore sizes <10.7 nm) relative to as-received sample for each thermochemically treated shale sample. The pore volume was obtained from the BJH PSD for the adsorption branch. The shale sample reference numbers are those given in Table 1.

both cases shown in Fig. 13, the overcondensation boundary desorption isotherm converges with the conventional desorption curve by a relative pressure of ~0.94. The location of this convergence point suggests that the large macropores detected by the overcondensation method must be shielded by only larger mesopores, and none by the smaller micro- and meso-pores of Network 1. This contrasts markedly with what has been found previously for Rempstone shale (Rigby et al., 2020a), where the convergence of the overcondensation isotherm with the conventional desorption happens at a much lower relative pressure of ~0.4–0.5, thereby suggesting large macropores are shielded by small mesopores and microporosity. The conventional desorption isotherm is thus just a descending scanning curve.

Since the gas overcondensation technique provides a complete

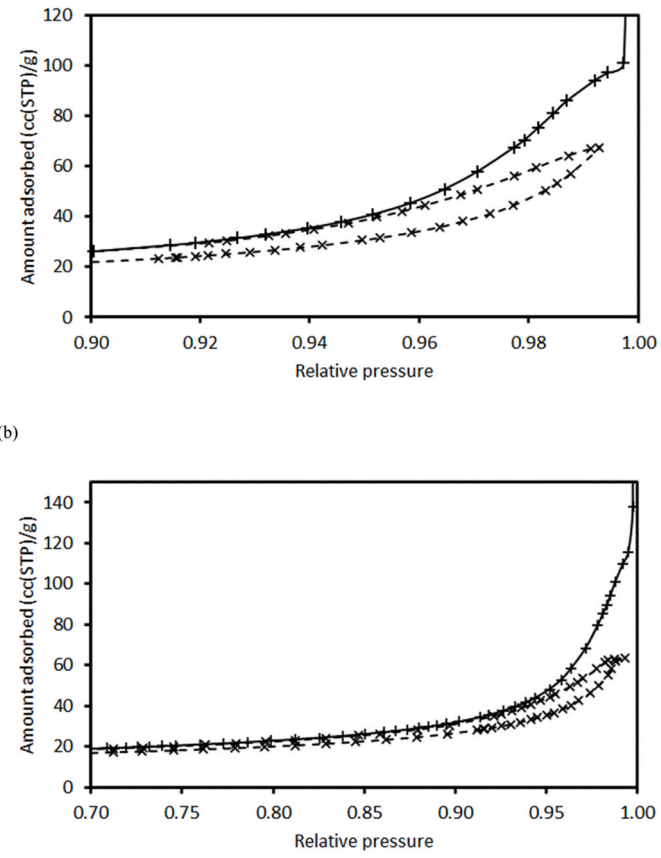

Fig. 13. A comparison of the overcondensation boundary desorption curves (+) with the conventional nitrogen sorption isotherms (×) for the as-received (a) and 1850 (b) shale samples, of particle sizes >150 μm.

boundary desorption isotherm, this can be analysed, in conjunction with the conventional adsorption isotherm, using percolation theory, to determine pore connectivity (Seaton, 1991; Rigby, 2020). Application of this procedure to the data shown in Fig. 13 suggested that the best fit, of the generalised scaling relation for a random pore bond network, to the experimental data was obtained when pore length was proportional to the inverse square of pore diameter. This suggests that the void space units with a larger characteristic dimension controlling capillary condensation are typically more compact in shape, while units with a smaller such dimension are more elongated. The pore connectivity and lattice size parameters for the untreated sample were 2.64 and 5.85, respectively, while the equivalent parameters for the 1850 treated sample were 2.53 and 6.32, respectively. This suggests that the 1850 treatment conditions have led to a slight decline in pore connectivity, and general network accessibility.

The amounts of nitrogen adsorbed at the knee and plateau in the overcondensation data can be converted into an estimate of pore volume by assuming that the adsorbed phase is liquid-like. The values obtained by this method for the as-received and 1850 samples were 0.156 cc/g and 0.178 cc/g, respectively, corresponding to an increase of 14% with treatment.

The specific pore volumes for all samples studied in this work were obtained gravimetrically using water saturation by vapour phase transfer. The values obtained by this method are shown in Table 5. It is noted that the pattern of changes in total pore volume with treatment conditions is different to that observed for Network 1 alone in Fig. 12. In particular, the total pore volumes for samples treated with added water did not all increase.

Together with the pore volumes for Network 1, given in Appendix 6, the total pore volumes, given in Table 5, can be used to estimate the pore volumes for Network 2 from the difference between the pair of values for each sample type. The pore volumes for Network 2 thus obtained are given in Table 5. The changes in Network 2 pore volume, for treated samples, relative to the untreated sample, have been correlated with the changes in mineral composition. It was found that the correlation of the change in biotite content with the relative change in the pore volume of Network 2 (corresponding to pores larger than 10.7 nm) was (marginally) statistically significant ($p = 0.05$). It is noted from Section 4.2.3 above that, in contrast, the changes in the pore volume of Network 1 (corresponding to pores smaller than 10.7 nm) were associated with changes in albite and smectite content. Hence, larger length-scale changes appear to be associated with biotite, while smaller length-scale changes are associated with albite and smectite.

5.3. Serial adsorption of nitrogen and iodononane combined with CXT

While the nitrogen sorption scanning curves have identified Network 1 as a separable component of the void space, the serial adsorption experiments described in this section will reveal its spatial distribution and association with a particular mineral phase. Fig. 14 shows conventional nitrogen sorption isotherms for a typical sample of as-received shale, of particle sizes >150 μm, before and after pre-adsorption with iodononane. It can be seen, on the linear plot, that the data for the empty sample shows a steep rise at low relative pressure, which on the log plot is associated with a step between relative pressures of ~0.001–0.01. The form of the multi-layer adsorption region for the empty sample is relatively linear in form on the linear plot. The hysteresis loop for the empty sample begins just above a relative pressure of 0.4. Between relative pressures of ~0.4 and ~0.8, the hysteresis loop is relatively narrow with the desorption branch running roughly parallel with the adsorption branch. After a relative pressure of 0.8, there is a steep rise in the boundary adsorption isotherm, and the width of the hysteresis loop increases. The top of the adsorption isotherm has the hyperbolic shape, and lack of a flat, horizontal plateau, that indicates that complete saturation of the sample with liquid nitrogen did not occur. (see Fig. 15)

In contrast, the isotherm for the sample after pre-adsorption with iodononane shows a much smaller, more rounded, initial step at low relative pressure than the empty sample. The reversible multi-layer build-up region extends over a much larger range of relative pressures for the sample containing iodononane, since the hysteresis only begins at a relative pressure of ~0.75–0.8. The hysteresis loop for the sample containing iodononane is relatively wide and has a similar shape to the high pressure end of the corresponding loop for the empty sample.

It is also noted that the iodononane pre-adsorption process fills the micropores and mesopores classified above as belonging to Network 1 only. It has been seen that pre-adsorption of iodononane in the as-received shale sample leads to a loss of access for nitrogen to the micropores and the mesopores normally filled in the region of the isotherm with the narrow hysteresis between parallel adsorption and desorption boundary curves. The residual nitrogen sorption isotherm following iodononane pre-adsorption has the simple Type IV form expected for multi-layer adsorption followed by capillary condensation in large mesopores and macropores. Therefore, it is proposed that, together, the scanning curve data and iodononane pre-adsorption data suggest that Networks 1 and 2 are thermodynamically independent pore systems within the shale. This means that the disposition of the two networks is such that the phase transitions associated with gas sorption can occur independently in each network. This, in turn, implies the transition in typical pore sizes at the mutual boundary of the two networks is sufficiently stark to prevent advanced condensation crossing this boundary, and that each network has a separate critical path to the exterior.

Modelling of the nitrogen adsorption isotherms obtained before and after iodononane adsorption was carried out using a single-component fractal BET model and the 2-component fBET + Henry's law homotattic patch model 8. The models were fitted to the range of 0–0.5 in relative pressure. Fig. 15 shows the results for a typical shale sample,

Table 5
Estimated total specific pore volumes for shale samples, measured via gravimetric method, together with corresponding estimated pore volume for Network 2.

Sample	Estimated total pore volume (cc/g)	Standard error (cc/g)	% change from as-received	Estimated Network 2 pore volume (cc/g)
As-received	0.154	0.007	0.0	0.128
1845	0.156	0.001	1.8	0.135
1846	0.112	0.001	−27.3	0.082
1847	0.147	0.003	−4.2	0.129
1849	0.181	0.007	17.9	0.162
1851	0.118	0.000	−23.4	0.099
1852	0.205	0.009	33.5	0.168
1853	0.143	0.007	−7.2	0.121
1854	0.155	0.008	0.7	–

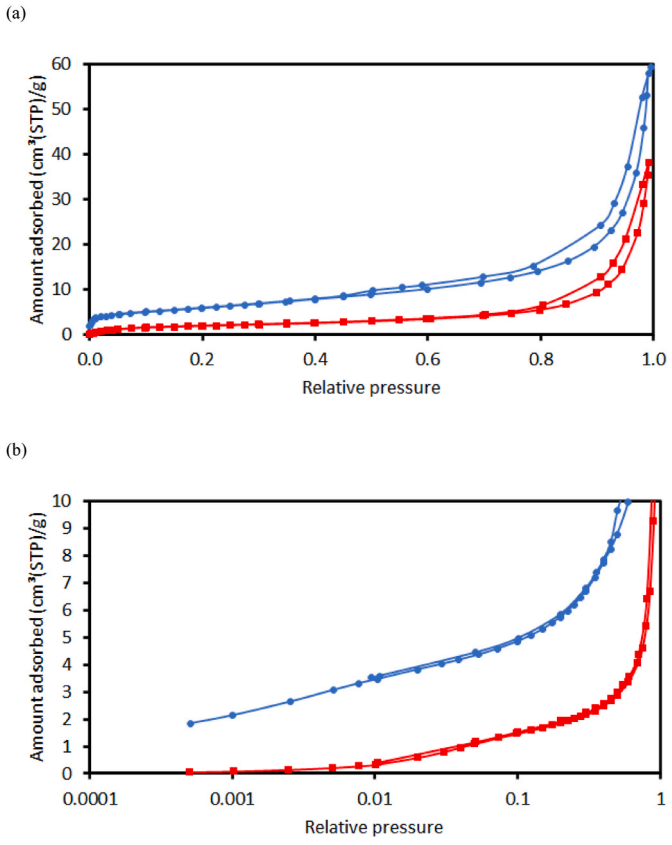

Fig. 14. Linear (a) and semi-logarithmic (b) plots of the nitrogen sorption isotherms acquired at 77 K for samples of as-received shale before (blue ●) and after (red ■) pre-adsorption with iodononane. (For interpretation of the references to colour in this figure legend, the reader is referred to the Web version of this article.)

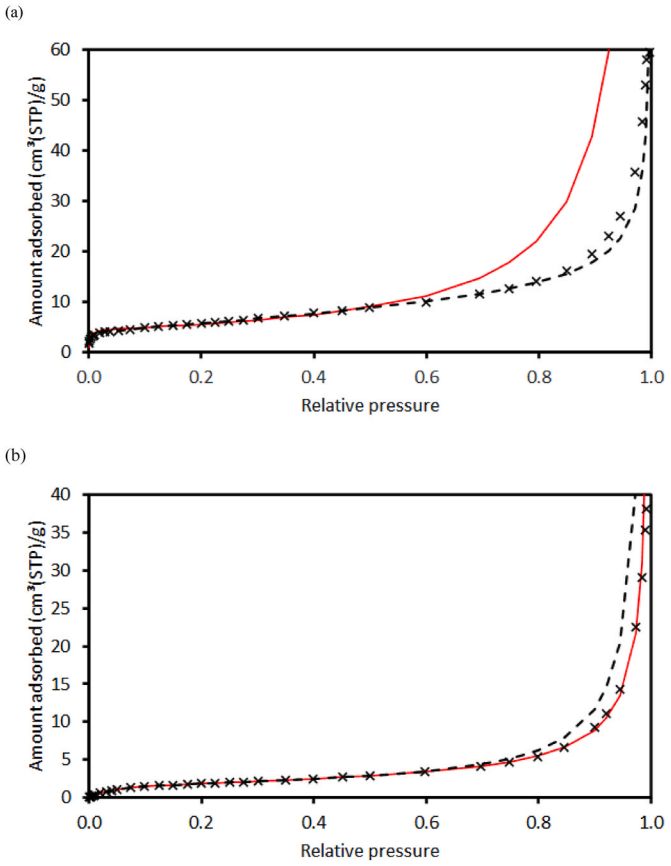

Fig. 15. Modelling of experimental nitrogen adsorption isotherms (×) for as-received shale chip sample #2 (see Table 6) obtained before (a) and (b) after iodononane adsorption. The solid red line is a fit of the data to a single fractal BET isotherm, while the dashed black line is a fit of the data to a 2-component fractal BET + Henry's law homotattic patch model. (For interpretation of the references to colour in this figure legend, the reader is referred to the Web version of this article.)

before and after iodononane adsorption, and it is clear that, before iodononane adsorption, the 2-component fBET + Henry's Law model fits the data better than the single fractal BET model. The single fractal BET models for samples before iodononane adsorption over-predicts the data at high pressures. However, after iodononane adsorption, the 2-component fBET + Henry's Law model performs worse than the single fractal BET model. The single component model fit is the same quality as for the more complex model at low pressures but better predicts the high-pressure section. To test repeatability between samples, nitrogen adsorption isotherms were obtained before and after iodononane adsorption on two different as-received shale chip samples. The parameters from the fits of the isotherm data to a 2-component fractal BET + Henry's Law model before iodononane, and a single component fractal BET model after iodononane, are shown in Table 6. It can be seen that the fitted parameters are very similar for each sample suggesting that repeatability is good.

From Table 6, it can be seen that the surface area from the fractal BET model after iodonanane adsorption corresponds to roughly that of one fractal BET component before iodononane adsorption, but the BET constant and fractal dimension for the single component model are both lower than for both their pre-iodononane pre-cursors in the homotattic patch model. The decline in apparent surface area is probably mostly due to the loss of accessibility of certain parts of the pore space due to adsorbed iodononane. However, previous work (Watt-Smith et al., 2005) has shown that nitrogen may also adsorb only on isolated patches if the surrounding surface has very low interaction strength. The decline in the BET constant and fractal dimension may be the result of iodononane filling microporous ruts in the surface of larger pores leading to an apparent smoothing of the surface and the loss of high surface

interaction strength sites.

Figs. 16 and 17 show examples of reconstructed two-dimensional slice CXT images through empty as-received shale chips, and as-received chips following iodononane pre-adsorption, respectively. To facilitate direct comparison between the images, they were all put on the same relative intensity scale using the X-ray absorbance of the air and the sample holder as internal references. Higher intensity in the image pixels corresponds to higher X-ray absorbance, and thus high density of the solid.

It can be seen in both sets of CXT images that chips have numerous very bright white dots corresponding to high X-ray absorbance of the same intensity in each case. From the MLA it is known the shale contains pyrite (density 5.01 g/cc), and these minerals are much denser than illite (density 2.75 g/cc), and thus the bright dots are probably pyrite mineral grains. The images also contain bright white pixels in linear features that are probably cracks contaminated with drilling mud containing barium. There are also bright white rings surrounding some voids. The intensity of the bright features is close to the maximum at 65,000. The mean intensity of voxels away from these bright white features was sampled in each image. This mean was taken over three 0.5 × 0.5 mm sampled areas from different 2D slices, as shown in Fig. 16a, and typical results are given in Table 7. From Table 7, it can be seen that the average intensity for empty as-received shale chips was found to be 24,851.

In addition, from Table 7, it can be seen that the typical pixel intensity of the shale matrix increased significantly following iodononane adsorption, since iodine is a heavy element with high electron density that absorbs X-rays. Further, while the CXT images of slices of as-received chips following iodononane pre-adsorption retain the scattering of bright white dots, they also exhibit darker patches of angular and ovoid shapes distributed within a brighter continuous matrix. A comparison of the grey-scale values of the image pixel intensities for the dark patches in the images of chips containing iodononane, with those for the continuous matrix region of the empty shale chips, found that they were identical within sampling error. However, the grey-scale values of the image pixel intensities of the continuous matrix phase in the chips containing iodononane were significantly elevated above those for the dark patches. These findings suggest that the iodononane adsorption has occurred only within the continuous matrix phase surrounding the dark patch regions. It is noted that the prevalence, shapes and sizes of the dark patch regions in the CXT images of chips following iodononane adsorption are similar to the grains of quartz and orthoclase seen in the MLA-SEM data in Appendix 3. The continuous matrix phase corresponds to the illite regions in the MLA-SEM data. The finding that quartz and orthoclase grains have low porosity, and are not accessed by probe fluid, is similar to what was also observed by Zhang et al. (2019).

5.4. Integrated gas sorption and mercury porosimetry combined with CXT

The characterisation described in this section will show the spatial distribution of the macropores of Network 2 and the particular mineral phase with which they are associated. It will also show how gas over-condensation can be used to show that high mercury intrusion pressures do not compress the sample mesopores. The raw data for the integrated experiment, consisting of the nitrogen sorption isotherms obtained before and after a mercury porosimetry experiment on the same sample, are given in Appendix 7. Fig. 18 shows these raw mercury porosimetry data analysed using the Kloubek (1981) correlations. It can be seen that the standard Kloubek (1981) correlations lead to a very near superposition of the extrusion curve upon the intrusion curve. Also shown is the retraction curve analysed using Kloubek-like correlations with slightly amended parameters, as given in Table 8. It can be seen that a minor modification of the original Kloubek (1981) parameters leads to a better superposition of the retraction curve on the intrusion curve. This suggests that the intrusion of, roughly, the upper two-thirds of the intrusion curve is reversible and entrapment only occurs in the largest third of pores. These findings also suggest that the mercury porosimetry hysteresis for the shale is dominated by contact angle hysteresis effects, since the near superposition obtained using the Kloubek correlations means that, more or less, the same width of hysteresis is found for the shale as for rigid controlled pore glass and sol-gel silica materials (Rigby, 2020). The dominance of the mercury contact angle effect means that the high pressure used in porosimetry is not itself responsible via potential elastic pore collapse (Rigby, 2020). This mechanical stability during high-pressure porosimetry also suggests the shale will not have deformed following extraction from the field.

Table 6
Parameters for 3-component (2 fractal BET + Henry's law) homotattic patch model for nitrogen adsorption isotherms before iodononane adsorption, and for single component fractal BET model fit after iodononane adsorption, for two as-received shale chip samples.

Isotherm model	Model parameters	Sample #1		Sample #2	
		Before	After	Before	After
Fractal BET #1	v_m1	2.17	1.93	2.15	1.86
	c_1	208.7	23.61	203.75	23.86
	d_1	2.53	2.31	2.51	2.32
Fractal BET #2	v_m2	2.01	N/A	1.94	N/A
	c_2	10316	N/A	10074	N/A
	d_2	2.56	N/A	2.51	N/A
Henry's Law	v_m3	3.11	N/A	3.19	N/A
	B	2.06	N/A	1.94	N/A

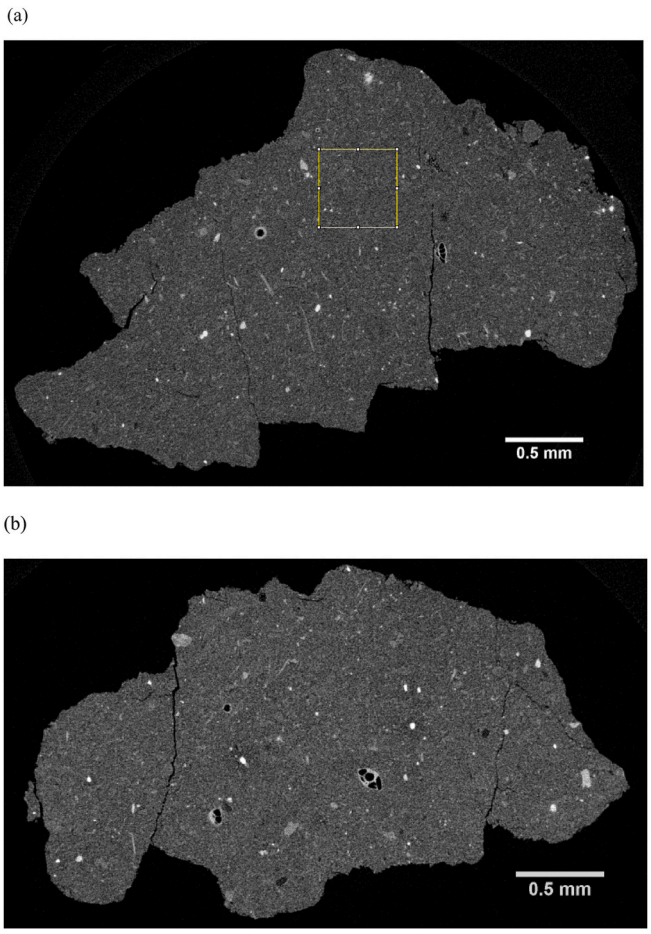

Fig. 16. Examples of reconstructed two-dimensional slice CXT images through empty as-received shale chips. Brighter white intensity corresponds to higher X-ray absorbance. The pixel resolution is 2.5 μm. The yellow square is an example of the regions for which the average pixel intensity was calculated. (For interpretation of the references to colour in this figure legend, the reader is referred to the Web version of this article.)

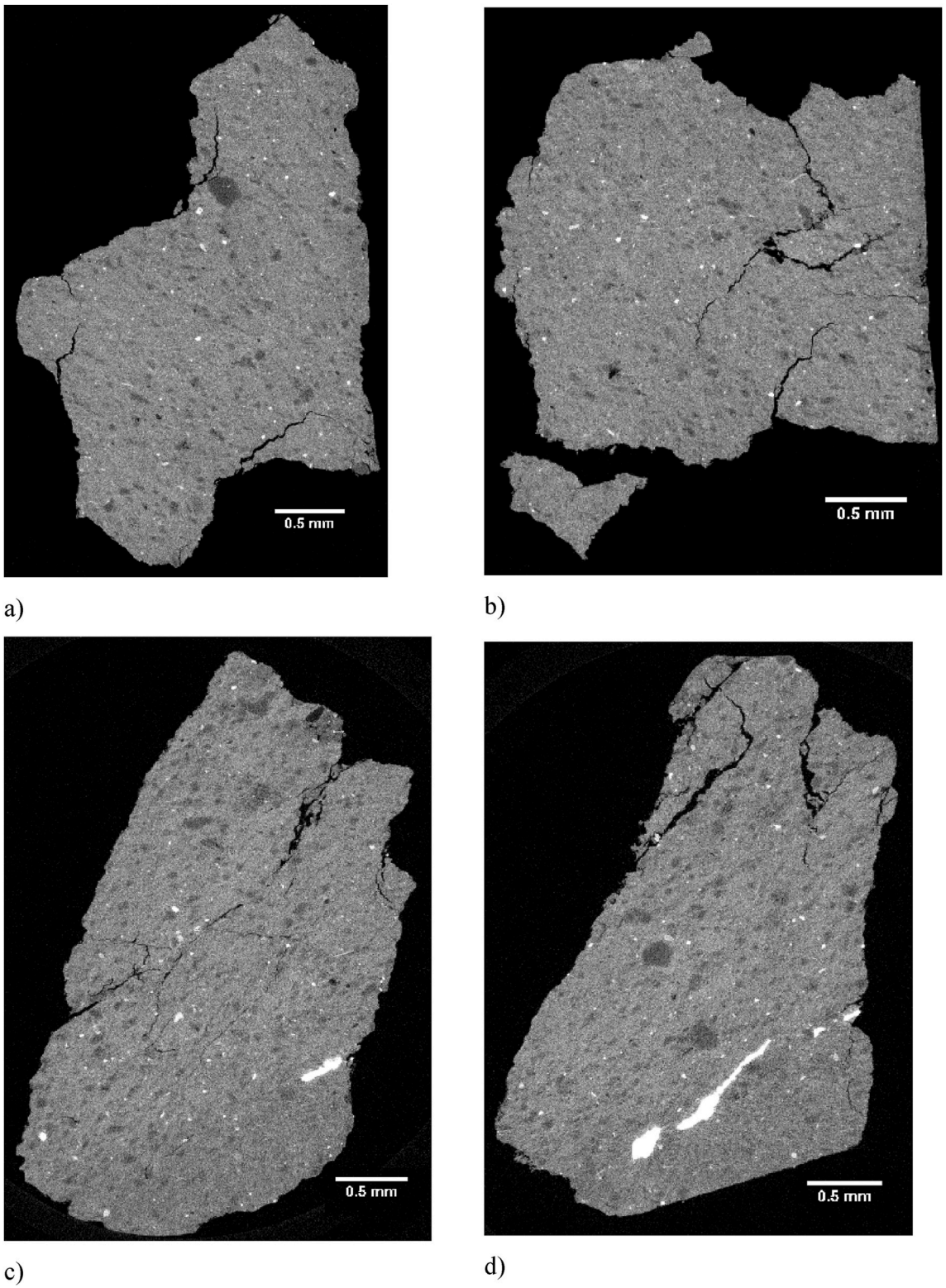

Fig. 17. Two-dimensional reconstructions from CXT images of samples of shale chips #1(a-b) and #2(c-d) following adsorption of iodononane. The images are on the same relative intensity scale as those in Fig. 16.

Fig. 19 shows the cumulative BJH PSDs derived from the nitrogen desorption branches of the isotherms, obtained before and after mercury entrapment, shown in Appendix 7. Also shown is the cumulative BJH PSD obtained from the nitrogen overcondensation boundary desorption isotherm for as-received shale powder with particle sizes >150 μm, and this PSD adjusted downward in cumulative volume by 0.07 cm^3/g. From Fig. 19, it can be seen that the PSDs for all three samples match for pore sizes below ~50 nm. Thereafter, for larger pore sizes the conventional isotherm PSDs diverge from the overcondensation PSD. This is because the conventional isotherms fail to detect capillary condensation in the largest pores. However, the PSDs from the conventional isotherms are consistent with mercury only becoming entrapped in the very largest pores.

Also shown in Fig. 19 is the mercury intrusion Kloubek (1981)

Table 7
The average image pixel intensity from examples of sampled areas (as seen in Fig. 16(a)) from CXT images for one empty as-received shale chip, and two different as-received shale chips following iodononane adsorption. (STD = standard deviation).

		Area 1	Area 2	Area 3	Average
As-received	Mean	24745	25151	24657	24851
	STD	5500	5397	5462	5453
Iodononane 1	Mean	41749	42160	42142	42017
	STD	5304	5413	5386	5367
Iodononane 2	Mean	37676	37427	37496	37533
	STD	5821	6282	6165	6089

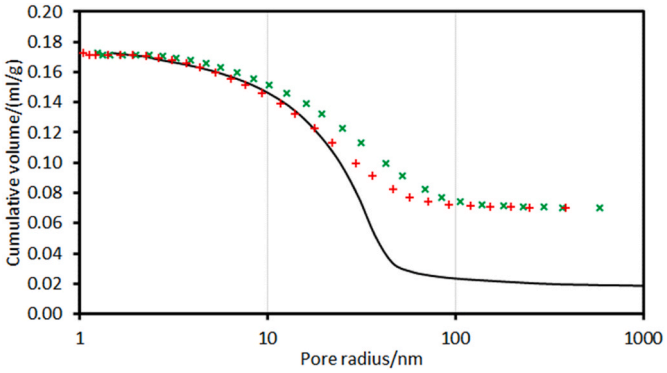

Fig. 18. Mercury intrusion curve (solid line) and extrusion curve (×) analysed using the standard Kloubek (1981) correlations, together with extrusion curve (+) analysed with amended Kloubek parameters given in Table 8.

Table 8
Amended Kloubek (1981) correlation parameters used to produce analysed mercury retraction curve shown in Fig. 18.

Kloubek parameter	Amended value
A	−45
B	−180

cumulative PSD with the ultimate intrusion volume at the smallest intruded pore size renormalised to the corresponding cumulative volume for the same pore size of the original overcondensation BJH PSD. It can be seen that the mercury intrusion PSD matches that of the nitrogen overcondensation for the smallest mesopores in the shale sample which require the highest mercury pressures to intrude. Some past workers (eg Garum et al., 2020) have proposed that mercury porosimetry should not be used with shales due to the high pressures involved leading to crushing of the sample. However, it is noted here that, while mercury porosimetry involves pressurising the sample to 414 MPa, the overcondensation and mercury intrusion PSDs match, and the nitrogen sorption PSD obtained following porosimetry matches that obtained before porosimetry, thereby suggesting that the pores are robust and do not collapse irreversibly under such pressure. The good agreement between the nitrogen overcondensation BJH PSD and mercury intrusion Kloubek (1981) PSD also mutually validates these respective data analysis methods, especially as it is achieved at the smallest pore sizes where the validity of the Young-Laplace approach to mercury porosimetry and Kelvin equation for gas sorption have been questioned (Rouquerol et al., 1999).

Fig. 20 shows examples of reconstructed two-dimensional slice CXT images through an empty as-received shale chip and an as-received chip following mercury entrapment. To facilitate direct comparison between the images, they were all obtained on the same relative intensity scale. Further CXT images of shale chips following mercury porosimetry are shown in Fig. 21. From Fig. 21, it can be seen that there are similar large irregular and small oval dark regions, with similar intensity to the unintruded chip, as found in the CXT images after iodononane

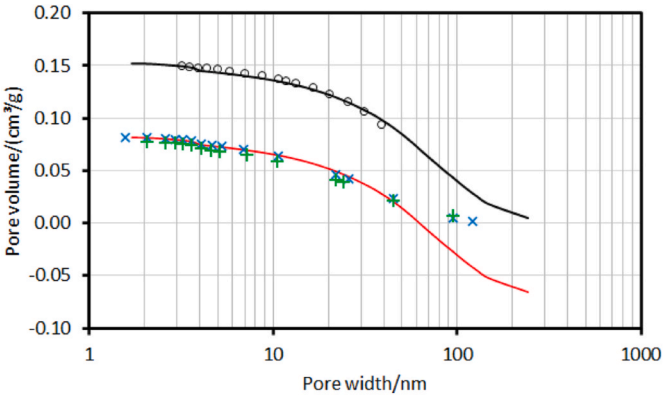

Fig. 19. BJH cumulative PSDs for as-received shale obtained from nitrogen desorption branch of overcondensation isotherm for fresh >150 μm powder (solid black line), conventional isotherm for chips before mercury entrapment (×), and conventional isotherm for chips after mercury entrapment (+). The solid red line is the overcondensation PSD with the pore volume adjusted for all data-points downward by 0.07 cm^3/g. Also shown (○) is the mercury intrusion Kloubek (1981) cumulative PSD with the ultimate intrusion at the smallest intruded pore size renormalised to the corresponding pore volume for the same pore size of the original overcondensation PSD. (For interpretation of the references to colour in this figure legend, the reader is referred to the Web version of this article.)

adsorption. These are, thus, probably also non-porous quartz and orthoclase grains, respectively, which do not intrude mercury and thus have no entrapment. Further, the rock matrix outside these dark regions has generally increased in X-ray absorbance following mercury entrapment, as it did following iodononane adsorption. However, there are also some differences between the respective CXT images after iodononane adsorption, and after mercury entrapment. The CXT images after mercury entrapment have small bright white patches not seen in the images of empty chips or chips following iodononane adsorption. These bright white patches are probably regions of mercury entrapment, as mercury strongly absorbs X-rays. Some of these new bright white patches seem to surround dark patches considered to be quartz or orthoclase grains. Loucks et al. (2012) classified various inter and intra-mineral grain pore structures through the use of SEM imaging, and found that interparticle pores can form around the rim of rigid quartz grains.

5.5. *Mass transport studies using gas uptake experiments*

As well as acting as a contrast agent to map the spatial distribution of Network 1 in CXT images, the pre-adsorbed iodononane can also act as a pore-blocking agent to 'filter-out' (exclude) the influence of Network 1 on mass transport. The kinetic mass uptake, of nitrogen gas at low relative pressure, by powder samples of as-received shale and treated shale, and shale chips before and after iodononane adsorption were obtained. Typically 2–3 samples were tested for each type of shale sample, and the sample means are reported. An example of a typical raw data-set from the nitrogen uptake experiment on a powder sample of as-received shale is shown in Fig. 22. It can be seen that there are two steps up in amount adsorbed occurring over two very different timescales. The first step corresponds to valve effects and pressure equilisation in the sample holder, while the second step is the uptake by the sample itself. Each data-set was fitted to 1-, 2- and 3-component LDF models as explained in the Theory section. In general, the 3-component gave the best fit. The mass transfer coefficient (MTC) parameters obtained from the LDF fits were corrected for adsorption, as described in the Theory section. The various batch averages for the weighted mean of the two LDF MTC components for the sample uptake itself are shown in Table 9.

From Table 9, it can be seen that, relative to the corresponding as-received shale sample of the same particle size, the mean MTC

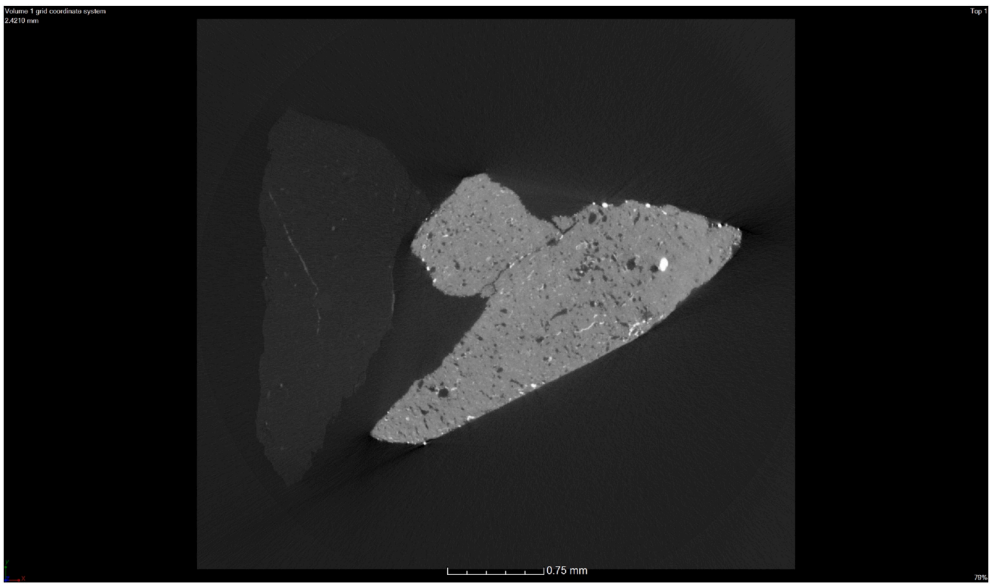

Fig. 20. Comparison of CXT 2D reconstructions of slices through as-received shale chips before and after mercury entrapment. The brighter chip (right) has mercury injected into the pores. The dim empty chip (left) is included for comparison.

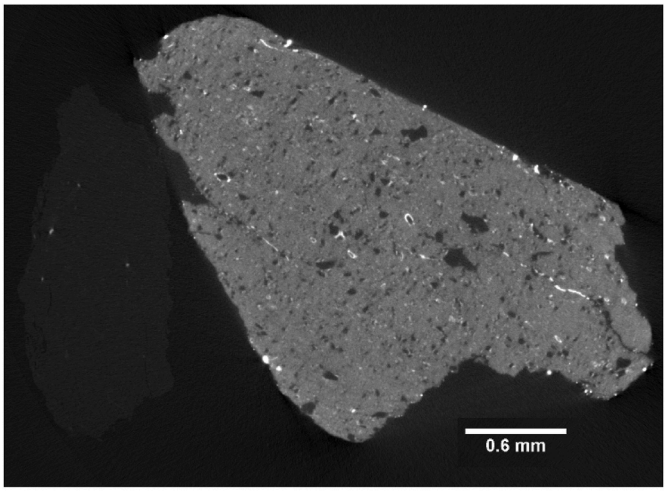

A)

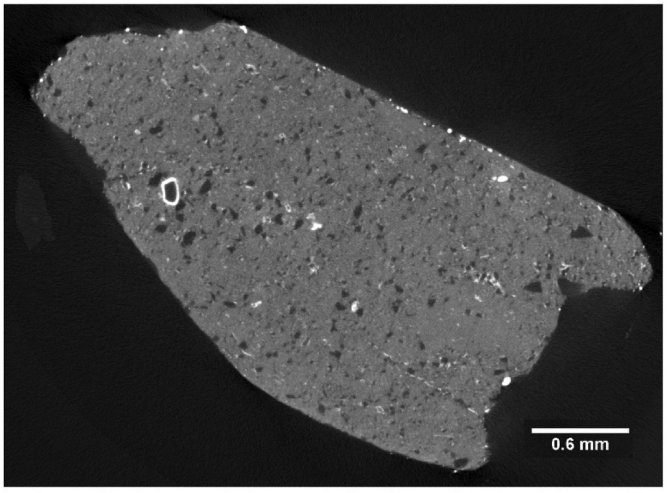

B)

Fig. 21. Computerised x-ray tomography images showing 2D slices (A and B) of shale chips after mercury injection.

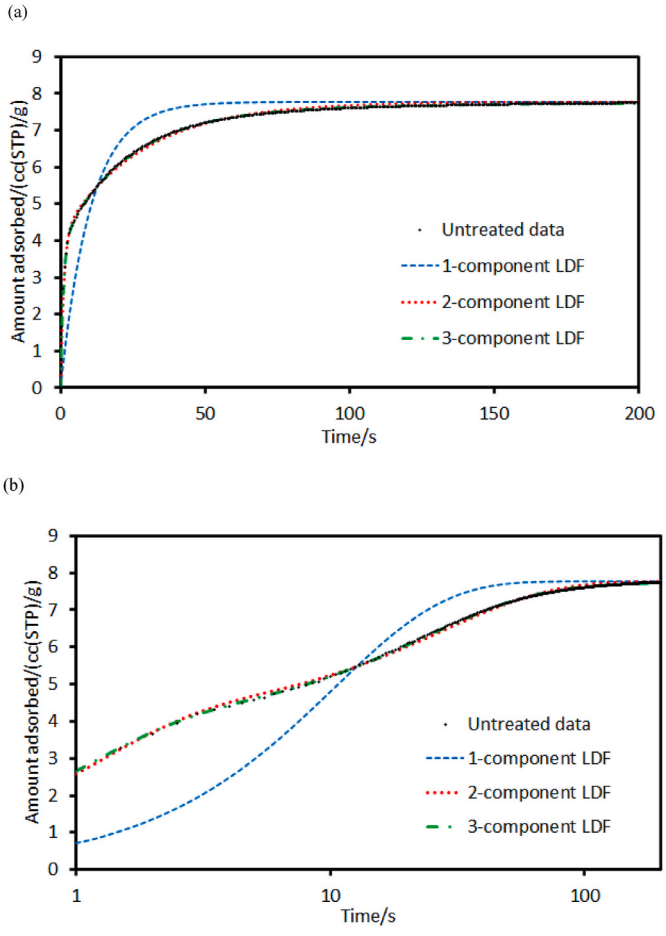

Fig. 22. An example of a typical raw data-set from the nitrogen uptake experiment on a powder sample of as-received shale shown on (a) linear and (b) semi-log co-ordinates. Also shown (lines) are fits to 1-, 2-, and 3-component LDF fits.

increased both following treatment and following iodononane adsorption. Since adsorption of iodononane reduces the available porosity, and thus effective diffusivity, then the increase in MTC must be associated with a decrease in the penetration depth into the shale samples. This means that the Network 1 porosity blocked by iodononane must be critical to percolating pathways through the shale.

The MTCs for the as-received and treated >150 μm powder samples were correlated with the parameters from the homotattic patch model parameters, given in Table 4, both individually, and using multiple linear regression (MLR). Only those homotattic patch model and other parameters that were shown by their pair-wise correlation coefficients to be independent of each other were selected for MLR. Given that the iodononane adsorption experiment has established that Network 1 is important for mass transport, then the pore volume for Network 1 in isolation was a parameter used in the MLR. MLR was conducted with both the absolute value and logarithm of each parameter to test both summation and power law correlations. MLR of the logarithms of homotattic patch model (Model 8) total surface area and the pore volume of Network 1, with the logarithm of the MTC, was found to give rise to a statistically-significant correlation ($F = 23.97$, $p = 0.0007$). However, it is noted that, in contrast, the corresponding MLR employing the ISO BET surface area instead did not give rise to a statistically-significant correlation ($p = 0.634$). This suggests that the ISO BET surface area may not be physically meaningful, and the homotattic patch surface area and Network 1 pore volumes are the key parameters determining the mass transport rates in the shales.

6. Discussion

The above findings have demonstrated a relationship between particular alterations to the shale pore structure, and associated changes to mass transport rates, resulting from accelerated treatment with $scCO_2$ with and without brine. The mineral liberation analysis (MLA) studies have shown a loss of biotite, albite and smectite following treatment, and, thus, a concomitant relative increase in illite. This suggests that treatment has led to the modification or dissolution of biotite, albite and smectite. The FTIR data suggested the illite had been carbonated as a result of treatment. These mineralogical changes are reflected in the variation in the parameters of the homotattic patch model fits to the nitrogen adsorption data for the treated samples, compared to the as-received sample. The addition of water led to a roughening of the shale following treatment, while extended treatment time led to a reduction of roughness for the dry CO_2 treated samples. The former may be due to acid-etching creating ruts, while the latter may be due to sintering smoothing the surface. The presence of swelling clays, such as smectite, which may trap some water, may explain the reactivity even of samples without added water.

The regression analysis of the changes, with thermochemical treatment, in mineralogy and shale surface area suggest that the change in the latter is at least partly associated with the plagioclase feldspar, and the mercury ring structures seen surrounding plagioclase grains in the CXT following porosimetry suggest that it is specifically the feldspar surfaces of inter-granular pores surrounding these non-porous grains. The regression analysis of the changes in Network 1 pore volume with changes in mineral composition following thermochemical treatment suggest the former is associated with changes in the albite and smectite content. It is likely that some of the smectite is modified to illite by the thermochemical treatment which may have changed the micro-/meso-pore volume. This particular mineral alteration might be anticipated as it is the process behind the illite/smectite geothermeter (Pollastro, 1990).

It has been seen that the combination with CXT of an indirect characterisation technique, such as adsorption or porosimetry, where the pore size penetrated by an X-ray contrast agent (such as mercury) is controlled, can be used to probe the macroscopic variation in nanoscopic properties (like mesopore size). Hence, statistically representative information on the spatial variation in nanoscopic properties can be obtained.

The intervention study of the selective pore-blocking of as-received shale using iodononane demonstrated the critical importance of the smaller micro- and meso-pores, denoted Network 1, to mass transport in Nordland shale. A consideration of the CXT and nitrogen sorption data obtained before and after iodononane pre-adsorption suggests that the iodononane adsorbed within micropores and small mesopores located within the illite phase alone. The nitrogen sorption isotherms obtained before and after iodononane adsorption suggested the iodononane adsorbed in the pores corresponding to the region of the isotherm belonging to Network 1, as identified from the nitrogen scanning curve data. Hence, Network 1 is spatially pervasive and continuous throughout the shale. Similarly, the CXT of shale samples after Network 2 had been selectively filled with entrapped mercury suggested it too was pervasive throughout the illite matrix. The change in MTC, from the kinetic mass uptake experiments following filling of Network 1 with iodononane, showed Network 1 was critical to overall mass transport, and it is likely that any mass transport flux had to pass through Network 1 pores at some stage. This is consistent with their spatially pervasive distribution seen in the CXT data. It is, thus, perhaps, then not surprising that the MLR found that the pore volume of Network 1 in a given batch was also needed to predict the MTC following treatment.

The combination of controlled ingress of X-ray contrast agent and CXT can be expanded to include scanning curve ingress of contrast agent to different pressures, thereby highlighting the spatial location and accessibility of void space regions with progressively different nanopore sizes (Rigby, 2020; Pini et al., 2021). This can be more readily achieved for much more statistically-representative volumes than multimodal imaging alone. It would also mean pore size distributions (PSDs) could be mapped with CXT, as with MRI, but for materials containing paramagnetic minerals. Indeed, the combination of mercury and iodononane contrast agents used here allows the separate mapping of the two tails of the PSD.

The MLR also showed that the homotattic patch model surface area was successful in predicting the MTC, while the surface area from the ISO BET method was not. This suggests that for materials as chemically and structurally complex as shales then a more sophisticated isotherm modelling approach, as adapted here, is essential to produce characteristic parameters, like surface area, that have physical meaning beyond simple fitting parameters, and thus are useful for further use in successful prediction. The characteristic parameters obtained here, such as the homotattic patch model surface area and Network 1 pore volume, are also statistically representative of much larger void volumes than is feasible with imaging methods alone.

The findings in this work suggest that, in order to deduce which particular structural changes are important and associated with the changes in mass transport properties for shales, it is essential to use more sophisticated characterisation methods and pore structure descriptors than are used in most past studies. The general increase in MTC with

Table 9
Batch mean mass transfer coefficients for shale samples.

Sample	Batch mean MTC/ s^{-1}	Standard error/ s^{-1}
As-received shale powder >150 μm	0.86	0.14
1845	1.26	0.24
1846	2.78	0.24
1847	1.34	0.17
1849	1.02	0.20
1851	2.26	0.06
1852	1.63	0.27
1853	1.95	0.37
1854	1.79	0.19
As-received empty shale chip	0.360	0.014
As-received chip following iodononane adsorption	0.630	0.172

treatment, irrespective of the addition of water, suggests the prolonged exposure of shale inter-layers and caprocks, like the Nordland shale, to $scCO_2$ will result in progressive increase in their permeability over time. For thin shale inter-layers this may affect the level of sideways deflection in plume migration. The various treatments all affected the pore volume of Network 1, albeit in different directions dependent upon conditions, and Network 1 has been seen to be pervasive throughout the percolating illite matrix, and thus the impact of the $scCO_2$ might be expected to progressively spread through this phase given its percolating nature, as seen in the CXT images. The much longer-range penetration of $scCO_2$ will depend upon whether this percolating property of the illite matrix Network 1 is retained over such length-scales, but this is beyond the scope of the work presented here. However, the iodononane pre-adsorption followed by CXT experiment could be performed on ever larger-sized samples. While it is not yet possible to determine the full impact on the sealing efficiency of thicker caprocks, the processes studied here will certainly be important for the thinner inter-layers. The overcondensation and CXT contrast agent methods used here are also applicable to other types of rocks, and have begun to be applied to Rempstone and Utica shales (Rigby et al., 2020a; Pitcher et al., 2021).

It has also been seen here that, since the gas overcondensation method can probe macroporosity, then percolation analysis can be applied, to nitrogen sorption data even for rocks, like shales, that possess a very wide range of pore sizes, to deliver estimates of pore connectivity. Pore connectivity is rarely considered for shales, and the over-condensation method, coupled with percolation analysis, provides a statistically-representative, convenient and quick method (relative to imaging) to obtain such information.

The results presented have shown that the use of more comprehensive and accurate void space characterisation, and resultant descriptors, enables more detailed and better information to be delivered on the impact of carbon dioxide on shale caprocks and inter-layers, since its true effects are then no longer obscured by limited and misleading void space descriptors, like the commonly used standard BET surface area. The alternative void space descriptors used here do not lead to the apparently conflicting findings found in some previous work. The methodology presented here should thus enable more confident prediction of the long-term plume behaviour of carbon dioxide and seal efficiency of caprocks.

Gas sorption scanning curves are presented here as an alternative, relatively novel (to geological applications), generally applicable tool for void space segmentation of complex rock structures that has a basis in a physical process, and key properties, of the real system, rather than the potentially more arbitrary and abstract algorithms used in image analysis. The physical meaningfulness of the units identified from the segmentation utilised has been validated by correlation with particular mineralogical changes and mass transfer properties. The coupled CXT and adsorption/porosimetry experiments show that the void space units, segmented in the way used here, can also still be visualised. The partition of the void space, using the proposed segmentation methodology, permits insight, even for complex shale materials, into the particular importance of specific void space zones and how they are idiosyncratically modified by the reaction with water and carbon dioxide.

The findings here specifically related to how the pore structure and mass transport properties of Nordland shale itself evolved with exposure to supercritical carbon dioxide were not previously available in the literature. They should, therefore, provide a basis for more informed future work on the impact of the shale interlayers on plume migration, and the seal efficiency, of the Sleipner field.

7. Conclusions

Since shales are such complex porous materials, special methods are needed to obtain void space descriptors that are sufficiently accurate, such that they are also physically meaningful parameters. This work has shown that the surface area from the ISO BET method is not predictive of mass transport, whereas that obtained from the more sophisticated homotattic patch model is. The mineralogical and CXT studies have suggested that the as-received Nordland shale largely consists of a continuous matrix of illite with grains of quartz and feldspar embedded within it at random. The gas sorption and mercury porosimetry data have shown that the void space of the shale can be deconvolved into two thermodynamically-independent regions, namely Network 1, consisting of the micro- and smaller meso-porosity, and Network 2 consisting of the macroporosity. Gas overcondensation has confirmed that the macroporosity missed by conventional adsorption comprises part of Network 2, and pore-to-pore co-operative interactions for these pores on the desorption isotherm are also confined within this network. Gas overcondensation has also confirmed that mercury porosimetry does not crush the smallest mesopores. It has been seen that pore-selective contrast agents can be used to map macroscopic pore size spatial distribution with CXT. Complementary CXT studies of the spatial distribution of iodononane and entrapped mercury within the shale suggested that, despite being thermodynamically-independent, both the aforementioned Networks are associated with the spatially-pervasive illite matrix, and the quartz and feldspar are non-porous. The rate of adsorption studies found that, despite the small pore sizes therein which might be expected to provide high resistance, Network 1 still forms part of the key percolating pathway through the shale that is critical for mass transport, since blocking it with iodononane meant that the penetration of gas into the shale matrix was heavily restricted. Despite being pervasive throughout the illite matrix, Network 2 does not thereby provide a potential 'bypass' route along 'highways' around high resistance Network 1 small pores, as might have been expected. It was found that thermochemical treatment altered minerals that affected the total surface area and pore volume comprising Network 1, that led to changes to mass transport rates. Hence, it is now known which key void space descriptors controlling mass transport at lower length-scales must be fed into hierarchical descriptions of shale over larger length-scales.

Credit author statement

Richard Seely Conceptualisation, Methodology, Validation, Formal analysis, Investigation, Writing - Original Draft. **Thomas J. Liddy** Validation, Investigation. **Christopher A. Rochelle** Conceptualisation, Methodology, Resources, Writing - Original Draft, Writing - Review & Editing, Supervision. **Robin S. Fletcher** Conceptualisation, Methodology, Resources, Writing - Original Draft, Writing - Review & Editing. **Sean P. Rigby** Conceptualisation, Methodology, Formal analysis, Resources, Data curation, Writing - Original Draft, Writing - Review & Editing, Supervision, Funding acquisition.

Declaration of competing interest

The authors declare that they have no known competing financial interests or personal relationships that could have appeared to influence the work reported in this paper.

Acknowledgements

This work was supported by the Engineering and Physical Sciences Research Council (EPSRC) [Grant Reference number EP/L016362/1].

Appendix A1

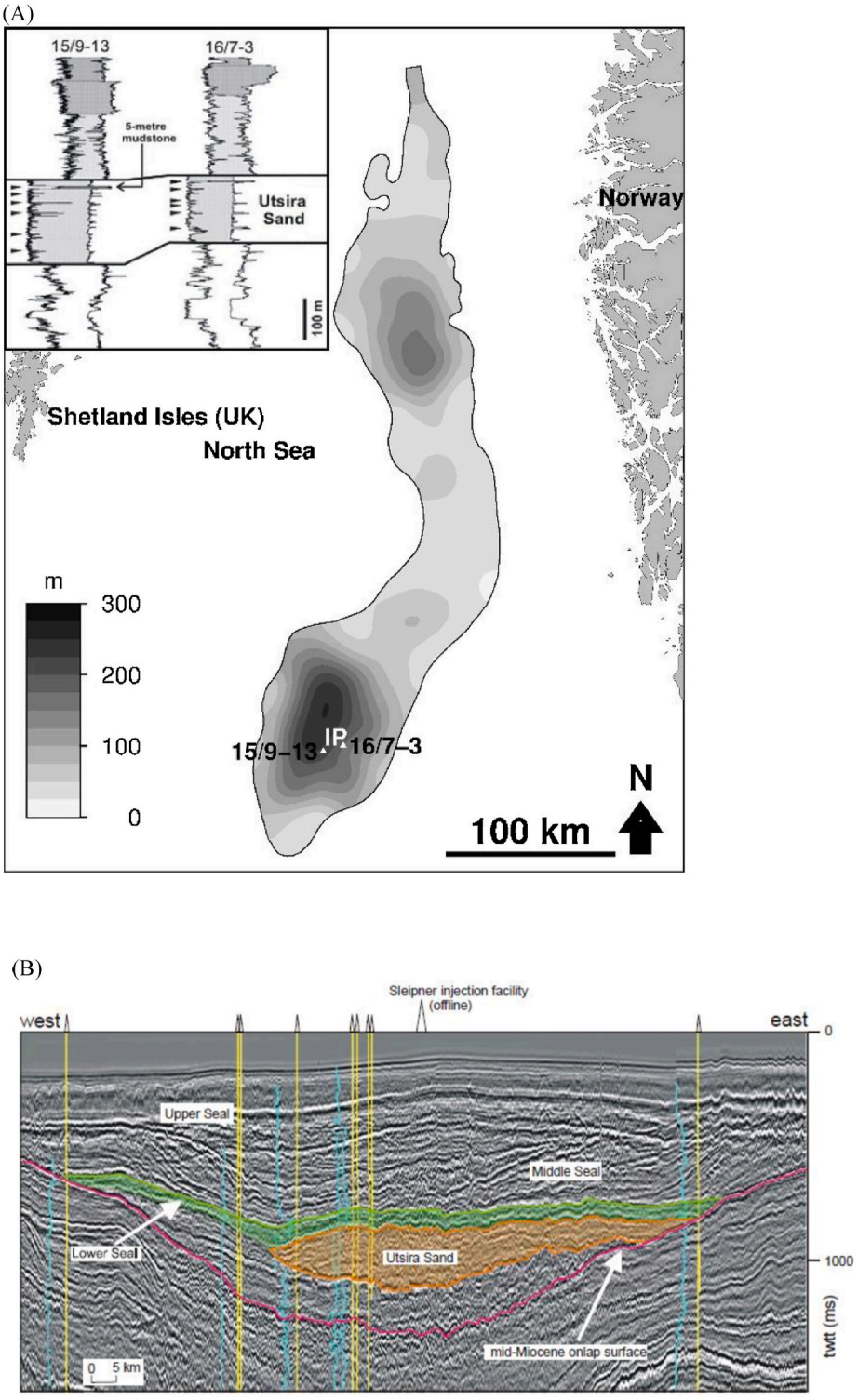

Fig. A1.1. (A) Isopach map of the Utsira Sand and (inset) representative geophysical well logs showing reservoir heterogeneity (γ-ray logs on the left tracks and resistivity logs on the right tracks). The reservoir sand has characteristically low γ-ray and resistivity readings so peaks within the sand denote thin mudstones. The topmost reservoir sand unit lies above the 5-m mudstone. IP = injection point. (reproduced under the terms of the Creative Commons CC-BY license from Williams and Chadwick (2021)); (B) Annotated seismic reflection section through the Sleipner area, with the key reservoir rock and caprock units highlighted (from the SACS2 project final report, Chadwick et al., 2002). 'twtt' = two-way travel time of the seismic signal, and here represents relative depth.

Appendix A2

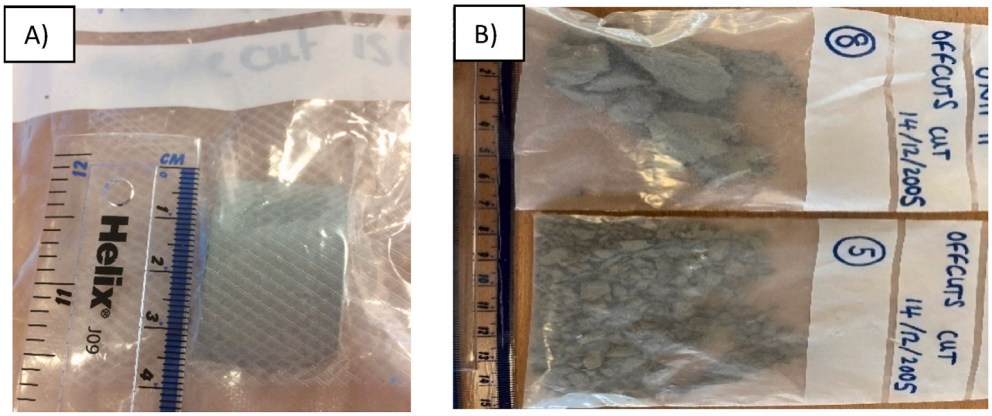

Fig. A2.1. Photographs of examples of Sleipner caprock samples received form the British Geological Survey (BGS). (A) Larger section, (B) Offcuts of varying size.

Appendix A3. MLA-SEM data

Figure A3.1A-D show samples of grain size <45-μm, 45-63-μm, 63-90-μm and 90-150-μm, respectively. Figure A3.1E shows a zoomed section of the <45-μm data. Figure A3.1E shows a base of illite making up the majority of the sample cross-section, interspersed with a variety of other minerals.

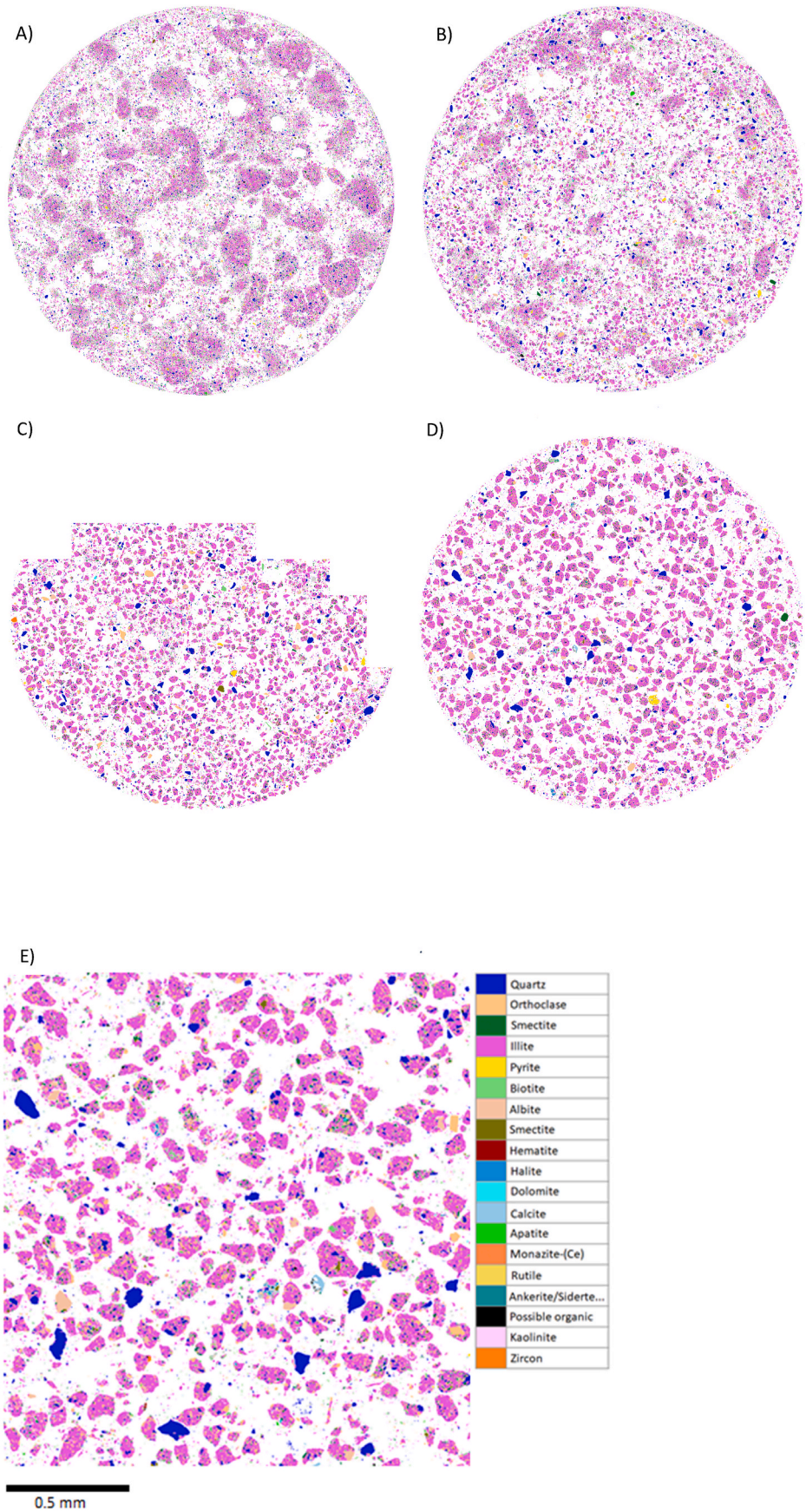

Fig. A3.1. MLA-SEM results after mineral phase segmentation and identification. Samples of grain size (A) < 45-μm, (B) 45-63-μm, (C) 63-90-μm and (D) 90-150-μm. Also shown is a zoomed section of the image in A (E). The empty white circles (such as near top of (B)) are due to manual post-processing to remove an air bubble. The diameter of the fields-of-view for (A)–(D) is 7 mm. The scale bar for (E) is 0.5 mm.

Figure A3.2 shows the modal mineralogy as a weight percentage for each as-received sample of different grain size. Only minerals which made up >0.1% of the samples are presented in Figure A3.2. However, several trace minerals were also found, but are not shown. The mineral content is generally similar for samples of different grain sizes but there are some differences as might be expected for heterogeneous shale rocks. For all as-received samples the most common mineral is illite. However, quartz, orthoclase, smectite, biotite, and albite are also abundant. It is also noted that, for some particular minerals, there are apparent systematic variations between samples. From Figure A3.2, it can be seen that as the shale sample particle grain size increases, there is some increase in illite and orthoclase content, and concomitant decrease in smectite and biotite. This could be due to a size selection effect for minerals during sieving, since grain size measurements for each mineral (not shown) suggested biotite had the smallest mineral grain size. Therefore, if grains of biotite were to detach from the bulk illite during the crushing process, it may fall through the sieves at a faster rate than the other minerals accumulating more in the smaller shale particle grain size samples. Hence, the majority of the analysis in the work is performed on the samples with the largest particle size.

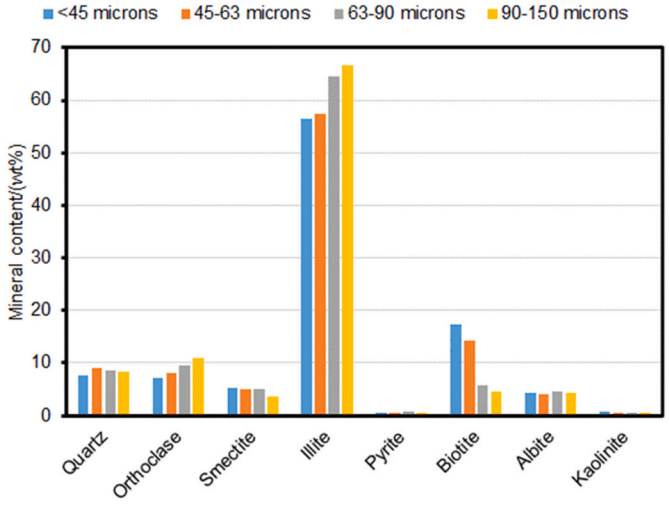

Fig. A3.2. MLA-SEM results for as-received shale samples with four different grain sizes ranges as shown in legend. Mineral contents are measured in weight percentage and only those of >0.1% are reported here.

Appendix A4. FTIR

Figure A4.1 shows the FTIR spectra for as-received shale, and for shale after treatment under sets of conditions 1851 and 1852. From Figure A4.1, it can be seen that, following treatment, peaks appear at 2973 (sh), 2935 and 2860 cm^{-1}. The peaks that appear at c.3000 cm^{-1} in the FTIR spectra for samples following treatment are likely to be the hydroxyl element of the carboxylic acid group, suggesting this group has been added to the shale as a result of treatment. The lack of change in IR spectra around 3000 cm^{-1} following treatment of plagioclase, albite and anorthite with wet and dry $scCO_2$ suggests it is not the feldspar in Nordland that is being carboxylated here (Loring et al., 2019). Sanguinito et al. (2018) and Goodman et al. (2019) studied the effects of $scCO_2$ on clays in Utica shale. FTIR results showed carbonate bands increased in intensity after CO_2 exposure. This happened rapidly within the first 15 min, and the magnitude of change was proportional to CO_2 pressure. Sanguinito et al. (2018) suggest carbonate precipitation and dissolution (mostly calcite) occurred until equilibrium was established. Quartz and pyrite were largely unaffected.

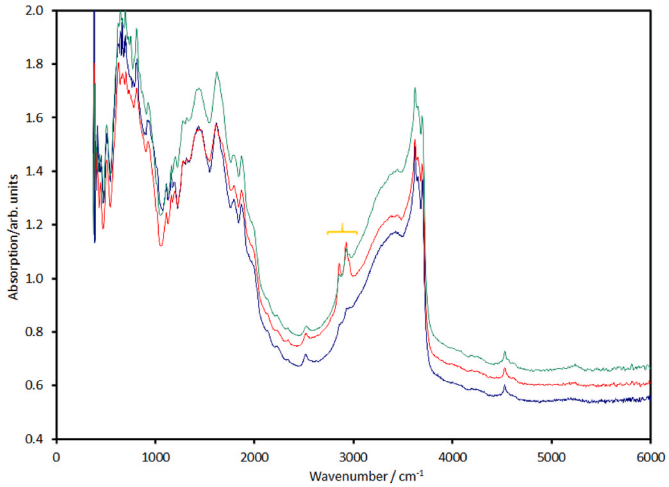

Fig. A4.1. DRIFTS spectra for as-received shale (blue), and treated shale samples 1851 (red) and 1852 (green). The orange bracket is to highlight that, following treatment, peaks appear at 2973(sh), 2935 and 2860 cm^{-1}.

Appendix A5. Gas adsorption data

Nitrogen sorption isotherms were obtained for a total of 19 samples of as-received shale, and are shown in Figure A5.1. The sample consisted of isotherms and repeats for shale samples in chip form, or samples in powder form with particle sizes in the ranges <53 μm, 90–150 μm, and >150 μm. Also shown in Figure A5.1 is the sample means isotherm and 95% confidence intervals on the mean. It can be seen that the confidence interval is a narrow range around the mean.

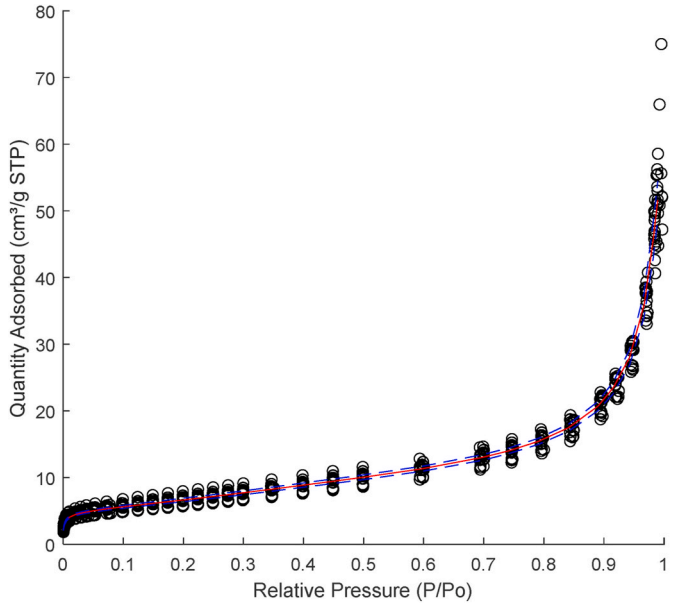

Fig. A5.1. Conventional nitrogen adsorption isotherms (○) for a total of 19 samples of as-received shale. Also shown are the sample mean isotherm (solid line) and 95% confidence intervals on the mean (dashed lines).

Table A5.1
BET specific surface areas obtained from nitrogen adsorption isotherms for treated and as-received samples.

Sample	ISO method BET surface area/(m^2g^{-1})
As-received >150μm powder 1	25.54 ± 0.03
As-received >150μm powder 2	25.14 ± 0.04
1845	18.53 ± 0.05
1846	27.73 ± 0.11
1847	17.51 ± 0.01
1849	20.60 ± 0.01
1850	34.17 ± 0.19
1851	15.46 ± 0.01
1852	34.21 ± 0.10
1853	22.87 ± 0.06

Appendix A6. Gas sorption scanning curve data

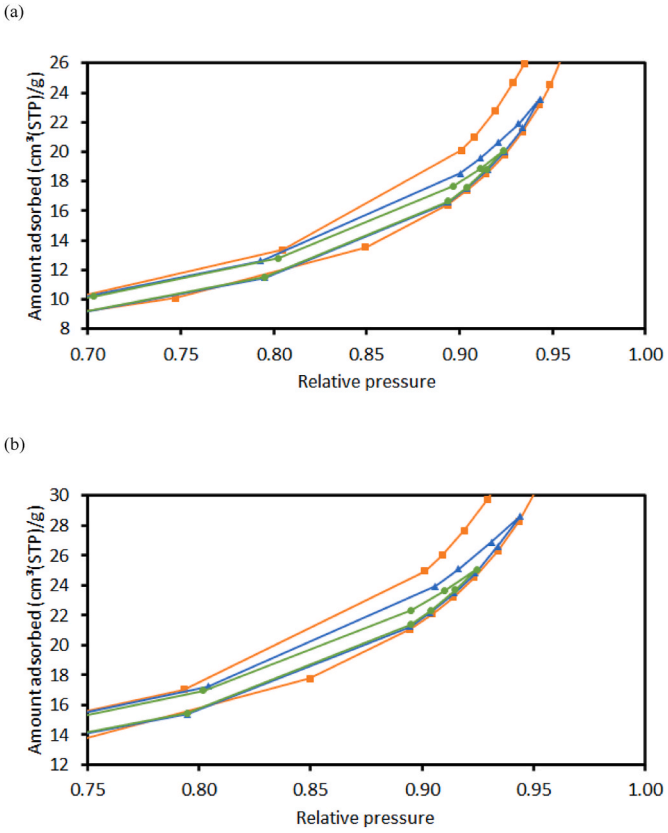

Fig. A6.1. Nitrogen sorption isotherms with desorption starting at ultimate relative pressures of 0.99 (■), 0.95(▲) and 0.93 (●) on the adsorption boundary isotherm for the (a) 1851 and (b) 1852 shale samples, of particle sizes >150 μm.

(a)

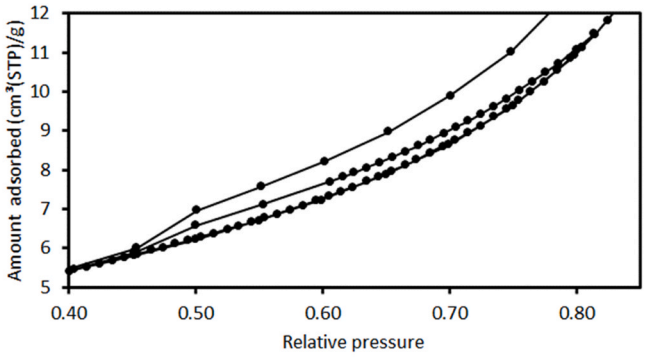

(b)

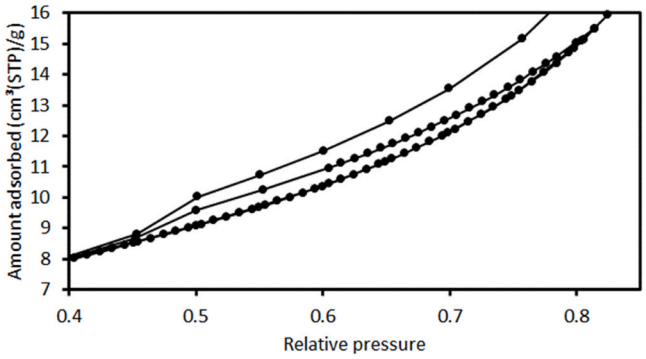

Fig. A6.2. Nitrogen sorption descending scanning curves starting at an ultimate relative pressure of 0.82 on the adsorption boundary isotherm for the (a) 1851 and (b) 1852 shale sample, of particle sizes >150 μm.

(a)

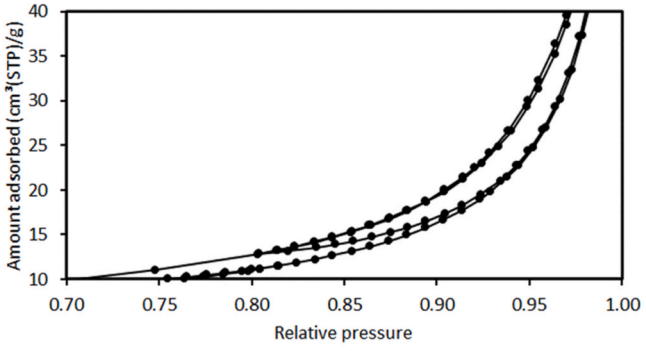

(b)

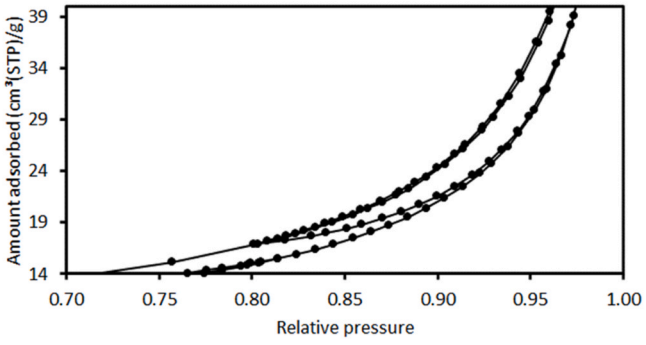

Fig. A6.3. Nitrogen sorption ascending scanning curves springing from an ultimate relative pressure of 0.8 on the conventional desorption boundary isotherm for the (a) 1851 and (b) 1852 shale samples, of particle sizes >150 μm.

Table A6.1
Pore volumes for Network 1 in each shale sample obtained from the BJH PSD for the adsorption branch. The shale sample names are those given in Table 1 in main text.

Shale sample	Network 1 pore volume/(ml/g)
As-received	0.0258
1845	0.0211
1846	0.0305
1847	0.0180
1849	0.0195
1850	0.0374
1851	0.0194
1852	0.0370
1853	0.0220

Appendix A7

Figure A7.1 shows the nitrogen sorption isotherms obtained before porosimetry, and after porosimetry with the amounts adsorbed at each point adjusted upwards by 1.02 $cm^3(STP)g^{-1}$. It can be seen that the adjusted adsorption isotherm overlays the unadjusted isotherm well for all relative pressures less than ~0.97. This suggests that the small loss of amount adsorbed after entrapment arises largely at the top of the capillary condensation region, with only a minor contribution in multi-layer region.

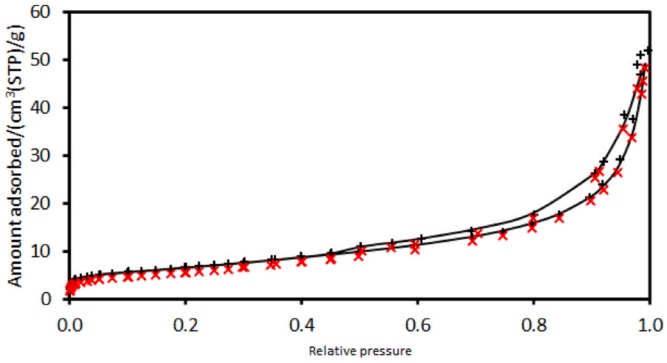

Fig. A7.1. Nitrogen sorption isotherms for as-received shale chips before (×) and after (+) mercury entrapment. The line shown is the sorption isotherms after entrapment with amount adsorbed for all data-points adjusted upwards by 1.02 $cm^3(STP)/g$.

In the raw mercury porosimetry data shown in Figure A7.2, the initial small step in intrusion at low pressure is due to mercury intrusion into the gaps between the sample chips. The second larger step represents intra-particle intrusion. On extrusion much of the mercury leaves the sample but there is some entrapment.

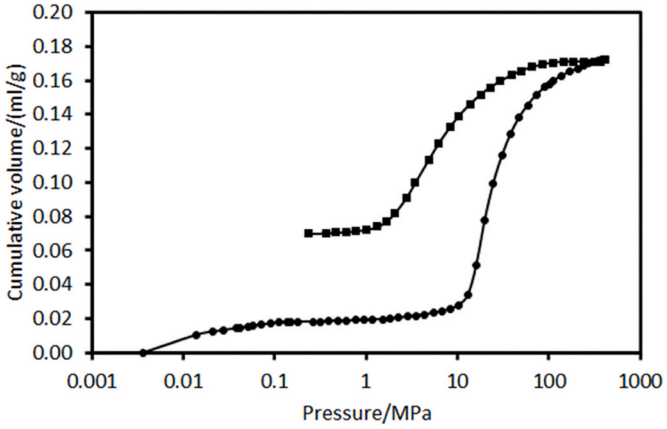

Fig. A7.2. Raw mercury intrusion (●) and extrusion (■) curves for as-received shale chips (lines shown are to guide the eye).

References

Ao, X., et al., 2017. Investigation on the physics structure and chemical properties of the shale treated by supercritical CO2. J. CO2 Util. 20, 274–281. https://doi.org/10.1016/j.jcou.2017.05.028.

Ardakani, O.H., et al., 2018. Do all fractions of organic matter contribute equally in shale porosity? A case study from Upper Ordovician Utica Shale, southern Quebec, Canada. Marin. Petrol. Geol. 92, 794–808. https://doi.org/10.1016/j.marpetgeo.2017.12.009.

Arif, M., Mahmoud, M., Zhang, Y., Iglauer, S., 2021. X-ray tomography imaging of shale microstructures: a review in the context of multiscale correlative imaging. Int. J. Coal Geol. 233, 103641.
International Standards Organisation (ISO), 2010. BS ISO 9277:2010 Determination of the Specific Surface Area of Solids by Gas Adsorption — BET Method. ISO, Switzerland.
Avnir, D., Farin, D., 1984. Molecular fractal surfaces. Nature 308, 261–263.
Barrett, E.P., Joyner, L.G., Halenda, P.P., 1951. The determination of pore volume and area distributions in porous substances. I. Computations from nitrogen isotherms. J. Am. Chem. Soc. 73 (1), 373–380.
Barsotti, E., Tan, S.P., Piri, M., Chen, S.P., 2020. Capillary-condensation hysteresis in naturally-occurring nanoporous media. Fuel 463, 116441.
Bateman, K., et al., 2013. Geochemical interactions between CO2 and minerals within the Utsira caprock: a 5-year experimental study. Energy Proc. 37, 5307–5314. https://doi.org/10.1016/j.egypro.2013.06.448.
Bickle, M., et al., 2007. Modelling carbon dioxide accumulation at Sleipner: implications for underground carbon storage. Earth Planet Sci. Lett. 255, 164–176. https://doi.org/10.1016/j.epsl.2006.12.013.
Bøe, R., Zweigel, P., 2001. Characterisation of the Nordland Shale in the Sleipner Area by XRD Analysis - A Contribution to the Saline Aquifer CO2 Storage (SACS) Project. SINTEF Petroleum Research Report No. 33.0764.00/01/01.
Chadwick, R.A., Kirby, G.A., Holloway, S., Gregersen, U., Johannessen, P.N., Zweigel, P., Arts, R., 2002. Saline Aquifer CO2 Storage (SACS2). Final Report: Geological Characterisation (Work Area 1). British Geological Survey Commissioned Report. CR/02/153C.
Eidvin, T., Jansen, E., Rundberg, Y., Brekke, H., Grogan, P., 2000. The upper Cainozoic of the Norwegian continental shelf correlated with the deep-sea record of the Norwegian Sea and the North Atlantic. Mar. Petrol. Geol. 17, 579–600.
Garum, M., Glover, P.W.J., Lorinczi, P., Drummond-Brydson, R., Hassanpour, A., 2020. Micro- and nano-scale pore structure in gas shale using X mu-CT and FIB-SEM techniques. Energy Fuel. 34, 12340–12353.
Gibbard, P.L., 1988. The history of the great northwest European rivers during the past three million years. Philos. Trans. R. Soc. London, Ser. A B 318, 559–602.
Goodman, A., et al., 2019. Investigating the role of water on CO2-Utica Shale interactions for carbon storage and shale gas extraction activities – evidence for pore scale alterations. Fuel 242, 744–755. https://doi.org/10.1016/j.fuel.2019.01.091.
Goodman, A., et al., 2020. Shale pore alteration: potential implications for hydrocarbon extraction and CO2 storage. Fuel 265, 116930. https://doi.org/10.1016/j.fuel.2019.116930.
Graham, A., Lonergan, L., Stoker, M., 2007. Evidence for late pleistocene ice stream activity in the witch ground basin, central North sea, from 3D seismic reflection data quaternary science. Review 26, 627–643.
Gregg, S.J., Sing, K.S.W., 1982. Adsorption, Surface Area and Porosity, second ed. Academic Press, London.
Hellmuth, K.H., Siitari-Kauppi, M., Klobes, P., Meyer, K., Goebbels, J., 1999. Imaging and analyzing rock porosity by autoradiography and Hg-porosimetry/X-ray computer tomography-applications. Phys. Chem. Earth Part A 24, 569–573.
Hill-Casey, F., Hotchkiss, T., Hardstone, K.A., Hitchcock, I., Novak, V., Schlepütz, C.M., Meersmann, T., Pavlovskaya, G.E., Rigby, S.P., 2021. Hyperpolarised xenon MRI and time-resolved X-ray computed tomography studies of structure-transport relationships in hierarchical porous media. Chem. Eng. J. 405, 126750.
Holzer, L., et al., 2010. 3D-microstructure analysis of hydrated bentonite with cryo-stabilized pore water. Appl. Clay Sci. 47, 330–342. https://doi.org/10.1016/j.clay.2009.11.045.
Jedli, H., et al., 2017. A laboratory study of supercritical CO2 adsorption on cap rocks in the geological storage conditions. Appl. Phys. Mater. Sci. Process 123 (4). https://doi.org/10.1007/s00339-017-0862-0.
Kaszuba, J., Yardley, B., Andreani, M., 2013. Experimental perspectives of mineral dissolution and precipitation due to carbon dioxide-water-rock interactions. Rev. Mineral. Geochem. 77 (1), 153–188. https://doi.org/10.2138/rmg.2013.77.5.
Kemp, S.J., Bouch, J., Murphy, H.M., 2001. Mineralogical Characterisation of the Nordland Shale, UK Quadrant 16, Northern North Sea. British Geological Survey Commissioned Report. CR/01/136. 52pp.
Klaver, J., Hemes, S., Houben, M., Desbois, G., Radi, Z., Urai, J.L., 2015. The connectivity of pore space in mudstones: insights from high-pressure Wood's metal injection, BIB-SEM imaging, and mercury intrusion porosimetry. Geofluids 15, 577–591.
Kloubek, J., 1981. Hysteresis in porosimetry. Powder Technol. 29 (1), 63–73.
Krushin, J.T., 1997. Seal capacity of non-smectite shale. AAPG Memoir 67. In: SURDAM, R.C. (Ed.), Seals, Traps and the Petroleum System, pp. 31–47.
Lahann, R., et al., 2013. Influence of CO2 on new albany shale composition and pore structure. Int. J. Coal Geol. 108, 2–9. https://doi.org/10.1016/j.coal.2011.05.004.
Liabastre, A.A., Orr, C., 1978. Evaluation of pore structure by mercury penetration. J. Colloid Interface Sci. 64, 1–18.
Liu, F., et al., 2012. CO2-brine-caprock interaction: reactivity experiments on Eau Claire shale and a review of relevant literature. Int. J. Greenh. Gas Control 7, 153–167. https://doi.org/10.1016/j.ijggc.2012.01.012.
Loring, J.S., Miller, Q.R.S., Thompson, C.J., Schaef, H.T., 2019. Chapter 4 - experimental studies of reactivity and transformations of rocks and minerals in water-bearing supercritical CO2. In: Newell, P., Ilgen, A.G. (Eds.), Science of Carbon Storage in Deep Saline Formations. Elsevier, pp. 63–88.
Lothe, A.E., Zweigel, P., 1999. Saline Aquifer CO2 Storage (SACS). Informal Annual Report 1999 of SINTEF Petroleum Research's Results in Work Area 1 'Reservoir Geology'. SINTEF Petroleum Research Report No. 23.4300.00/03/99.
Loucks, R.G., Reed, R.M., Ruppel, S.C., Hammes, U., 2012. Spectrum of pore types and networks in mudrocks and a descriptive classification for matrix-related mudrock pores. AAPG Bull. 96 (6), 1071–1098.
Lundegard, P.M., Samuels, N.D., 1980. Field classification of fine-grained sedimentary rocks. J. Sediment. Petrol. 50, 781–786.
Ma, L., Dowey, P.J., Rutter, E., Taylor, K.G., Lee, P.D., 2019. A novel upscaling procedure for characterising heterogeneous shale porosity from nanometer-to millimetre-scale in 3D. Energy 181, 1285–1297.
Mahnke, M., Mögel, H.J., 2003. Fractal analysis of physical adsorption on material surfaces. Colloids Surf., A 216, 215–228.
Mayo, S., Josh, M., Nesterets, Y., Esteban, L., Pervukhina, M., Clennell, M.B., Maksimenko, A., Hall, C., 2015. Quantitative micro-porosity characterization using synchrotron micro-CT and xenon K-edge subtraction in sandstones, carbonates, shales and coal. Fuel 154, 167–173.
Moreau, J., Huuse, M., 2014. Infill of tunnel valleys associated with landward-flowing ice sheets: the missing Middle Pleistocene record of the NW European rivers? G-cubed 15, 1–9.
Mouzakis, K.M., et al., 2016. Experimental study of porosity changes in shale caprocks exposed to CO2 -saturated brines I: evolution of mineralogy, pore connectivity, pore size distribution, and surface area. Environ. Eng. Sci. 33 (10), 725–735. https://doi.org/10.1089/ees.2015.0588.
Murray, K.L., Seaton, N.A., Day, M.A., 1999. An adsorption-based method for the characterization of pore networks containing both mesopores and macropores. Langmuir 15, 6728–6737.
Ng, K.C., Burhan, M., Shahzad, M.W., Bin Ismail, A., 2017. A universal isotherm model to capture adsorption uptake and energy distribution of porous heterogeneous surface. Sci. Rep. 7, 10634.
Pan, Y., Hui, D., Luo, P., Zhang, Y., Sun, L., et al., 2018. Experimental investigation of the geochemical interactions between supercritical CO2 and shale: implications for CO2 storage in gas-bearing shale formations. Energy Fuel. 32 (2), 1963–1978. https://doi.org/10.1021/acs.energyfuels.7b03074.
Pini, R., Joss, L., Hejazi, S.A.H., 2021. Quantitative imaging of gas adsorption equilibrium and dynamics by X-ray computed tomography. Adsorption 27, 801–818.
Pitcher, E.G., Large, D.J., Fletcher, R.S., Rigby, S.P., 2021. Multi-scale pore structural change across a paleodepositional transition in Utica shale probed by gas sorption overcondensation and scanning. Mar. Petrol. Geol. 134, 105348.
Pollastro, R.M., 1990. The Illite/Smectite Geothermometer—Concepts, Methodology, and Application to Basin History and Hydrocarbon Generation, 19/11/21. https://archives.datapages.com/data/rocky_sepm/data/028/028001/1_rocky_mount280001.htm.
Rigby, S.P., 2000. New methodologies in mercury porosimetry. In: Rodriguez-Reinoso, F., | McEnaney, B., Rouquerol, J. (Eds.), Characterization of Porous Solids VI (COPS-VI), vol. 144. Stud Surf Sci Catal, pp. 185–192.
Rigby, S.P., 2018. Recent developments in the structural characterisation of disordered. Mesoporous Solids. JMTR 62 (3), 296–312.
Rigby, S.P., 2020. Structural Characterisation of Natural and Industrial Porous Materials: A Manual. Springer International Publishing, Cham.
Rigby, S.P., Jahan, H., Stevens, L., Uguna, C., Snape, C., Macnaughton, B., Large, D.J., Fletcher, R.S., 2020a. Pore structural evolution of shale following thermochemical treatment. Mar. Petrol. Geol. 112, 104058.
Rigby, S.P., Stevens, L., Meersmann, T., Pavloskaya, G.E., Rees, G.J., Henderson, J., Bryant, S.J., Edler, K.J., Fletcher, R.S., 2020b. Structural and chemical heterogeneity in ancient glass probed using gas overcondensation, X-ray tomography, and solid-state NMR. Mater. Char. 167, 110467.
Rouquerol, F., Rouquerol, J., Sing, K., 1999. Adsorption by Powders and Porous Solids: Principles, Methodology and Applications. Academic Press, London.
Saif, T., Lin, Q., Butcher, A.R., Bijeljic, B., Blunt, M., 2017. Multi-scale multi-dimensional microstructure imaging of oil shale pyrolysis using X-ray micro-tomography, automated ultra-high resolution SEM, MAPS Mineralogy and FIB-SEM. Appl. Energy 202, 628–647.
Sanguinito, S., et al., 2018. Quantifying Dry Supercritical CO2-induced Changes of the Utica Shale, vol. 226, pp. 54–64. https://doi.org/10.1016/j.fuel.2018.03.156. Fuel.
Seaton, N.A., 1991. Determination of the connectivity of porous solids from nitrogen sorption measurements. Chem. Eng. Sci. 46 (8), 1895–1909.
Seemann, T., Bertier, P., Krooss, B.M., Stanjek, H., 2017. Water vapour sorption on mudrocks. Geomechanical and Petrophysical Properties of Mudrocks. Geol. Soc. 454, 201–234. London, Special Publications.
Sejrup, H.P., Aarseth, I., Haflidason, H., 1991. The quaternary succession in the northern North sea. Mar. Geol. 101, 103–111.
Stoker, M.S., Bent, A.J.A., 1987. Lower Pleistocene deltaic and marine sediments in boreholes from the central North Sea. J. Quat. Sci. 2, 87–96.
Thommes, M., Katsumi, K., Neimark, A.V., et al., 2015. Physisorption of gases, with special reference to the evaluation of surface area and pore size distribution (IUPAC Technical Report). Pure Appl. Chem. 87 (9–10), 1051–1069.
Tompsett, G.A., Krogh, L., Griffin, D.W., Conner, W.C., 2005. Hysteresis and Scanning Behavior of Mesoporous Molecular Sieves, 21, pp. 8214–8225.
Walker, W.C., Zettlemoyer, A.C., 1948. A dual-surface BET adsorption theory. Y. Phys. Colloid Chem. 52, 47–58.
Washburn, E.W., 1921. The dynamics of capillary flow. Phys. Rev. 17 (3), 273–283.
Watt-Smith, M., Edler, K.J., Rigby, S.P., 2005. An experimental study of gas adsorption on fractal surfaces. Langmuir 21 (6), 2281–2292.
Williams, G.A., Chadwick, R.A., 2021. Influence of reservoir-scale heterogeneities on the growth, evolution and migration of a CO2 plume at the Sleipner Field, Norwegian North Sea. Int. J. Greenh. Gas Control 106, 103260.
Wu, T., Li, X., Zhao, J., Zhang, D., 2017. Multiscale pore structure and its effect on gas transport in organic-rich shale. Water Resour. Res. 53, 5438–5450.

Yin, H., et al., 2016. Physical and structural changes in shale associated with supercritical CO2 exposure. Fuel 184, 289–303. https://doi.org/10.1016/j.fuel.2016.07.028.
Zhang, Y., Mostaghimi, P., Mostaghimi, P., Fogden, A., Sheppard, A., Arena, A., Middleton, J., Armstrong, R.J., 2018. Time-Lapsed visualization and characterization of shale diffusion properties using 4D X-ray microcomputed tomography. Energy Fuel. 32, 2889–2900.
Zhang, Y., Mostaghimi, P., Armstrong, R.J., 2019. Multiscale characterization of shale diffusivity using time-lapsed X-ray computed tomography and pore-level simulation. J. Petrol. Sci. Eng. 182, 106271.